Research Square

Preprints are preliminary reports that have not undergone peer review.
They should not be considered conclusive, used to inform clinical practice,
or referenced by the media as validated information.

Bovine viral diarrhea virus (BVDV) relies on cellular lipid droplet biogenesis and lipolysis to provide energy for viral replication

Xiaoran Xiong
China Agricultural University
Yi Liu
China Agricultural University
Yaohong Zhu
China Agricultural University
Jiufeng Wang
jiufeng_wang@hotmail.com
China Agricultural University
Guiyan Yang
China Agricultural University

Research Article

Keywords: Bovine viral diarrhea virus, Core protein, Lipolysis, Mitochondria, Fatty acid oxidation, Viral replication

Posted Date: June 29th, 2026

DOI: https://doi.org/10.21203/rs.3.rs-10059481/v1

License: This work is licensed under a Creative Commons Attribution 4.0 International License.
Read Full License

Additional Declarations: No competing interests reported.

Version of Record: A version of this preprint was published at Veterinary Research on September 19th, 2026. See the published version at https://doi.org/10.1186/s13567-026-01834-7.

Abstract

Bovine viral diarrhea virus (BVDV), one of the most important viral pathogens in cattle, causes serious economic losses due to immunosuppression and persistent infections. Previous studies have shown a tight connection between virus infection and lipid metabolism, particularly in the formation and degradation of lipid droplets. However, the pathogenic mechanism of BVDV infection and the molecular mechanisms by which viral proteins reprogram lipid metabolism remain unclear. We found that BVDV increased cellular lipid droplets (LDs) accumulation by enhancing the production of new lipids, accelerating exogenous fatty acid uptake, and elevating DGAT-dependent esterification of fatty acids (FAs). The generated LDs subsequently release free fatty acids (FFAs) via ATGL/HSL-dependent lipolysis. This lipolysis-dependent release of FFAs is accelerated and transferred to mitochondria for oxidation by increasing contact between LDs and mitochondria, thereby promoting viral replication. Furthermore, BVDV Core protein targets the surface of LDs, increasing and recruiting FASN and ATGL to promote LD mobilization. Meanwhile, the Core protein interacts with mitochondria, linking mitochondria to LDs and facilitating the release of FAs for efficient fatty acid oxidation. Collectively, this study demonstrates that the BVDV Core protein regulates cellular lipid metabolism to support BVDV replication, contributing to understanding the pathogenetic mechanisms by which BVDV interacts with host cells.

Introduction

Bovine viral diarrhea virus (BVDV) is one of the most important viral pathogens of cattle worldwide. It is an enveloped, single-stranded, positive-sense RNA virus belonging to the genus *Pestivirus* within the family *Flaviviridae*, which encodes a large polyprotein that undergoes proteolytic cleavage to form the structural proteins Core, Erns, E1, and E2 and nonstructural proteins Npro, P7, NS2, NS3, NS4A, NS4B, NS5A, and NS5B [1]. Infection with BVDV can cause mucosal necrosis and reproductive disorders in cattle [2]. The prevalence of BVDV infection in different geographic regions ranges from 28% to 66% in cattle herds, with 0.5% to 2.5% of livestock persistently infected (PI) with the virus [2]. Due to immunosuppression and high genomic variability, which enable rapid adaptation and persistent infection within herds, the emergence of new subtypes and reduced efficiency of vaccines lead to severe economic losses [3]. BVDV relies on host cellular factors and machinery to complete its life cycle, involving complex interactions with cellular lipid metabolism [4]. Despite their role as dynamic hubs of lipid and energy homeostasis, the involvement of lipid droplets (LDs) in BVDV infection remains undefined.

LDs are cellular organelles composed of a neutral lipid core and surrounded by a phospholipid monolayer decorated with a specific set of proteins [5]. LD biogenesis begins in the endoplasmic reticulum (ER), where the diacylglycerol acyltransferase (DGATs) enzymes esterify fatty acids (FAs) from either de novo lipogenesis (DNL) or exogenous uptake into TAG deposited between the leaflets of the ER bilayer [5]. LDs can be mobilized by releasing free fatty acids (FFAs) via lipophagy and lipolysis [6]. In lipophagy, LDs are delivered to autolysosomes or lysosomes for degradation by lysosomal acid lipase

(LAL) [6]. In lipolysis, cytosolic neutral lipases bind to the surface of the LDs to hydrolyze triacylglycerols [6].

Viral infections often correlate with accelerated LD biogenesis or catabolism. Fatty acids derived from LDs comprise the cellular FAs pool that performs several functions and is co-opted by diverse viruses for various purposes: (i) producing phospholipids for viral replication organelles (ROs); (ii) modifying viral protein by palmitoylation; (iii) re-esterifying to LDs for infectious virus assembly or providing substrates for fatty acid oxidation (FAO) to produce ATP [7]. These studies indicate that lipid metabolic reprogramming and LD formation may play crucial roles in the pathophysiology and replication of BVDV.

LDs are in contact with many organelles and provide the necessary lipids for biogenesis [5]. Beta-oxidation of fatty acids in mitochondria dominates the process of energy production [8]. Cellular FAs are activated into acyl-CoA and transported to the mitochondria via the carnitine cycle. Within the mitochondria, they are then progressively degraded to produce energy through a series of cyclical reactions that include dehydrogenation, hydration, another dehydrogenation, and finally thiolytic cleavage [8]. LDs can dynamically associate with subpopulations of mitochondria in different cell types or under different metabolic conditions [9]. Contacts between LDs and mitochondria could serve as sites for both lipogenesis and lipolysis. However, whether BVDV infection regulates mitochondrial function for β-oxidation and the contact between LDs and mitochondria remains largely unknown.

LDs and mitochondria have a recognized involvement in the life cycle of *Flaviviridae* family viruses. The capsid proteins of Hepatitis C virus, Dengue Virus, and Zika virus from the *Flaviviridae* family bind to the LDs via relatively conserved residues. These viruses usurp the LDs and alter the lipidomic profiles and lipid droplet-associated innate immunity to enhance their viral processes [10–12]. Other viral proteins from the *Flaviviridae* family have been shown to localize to mitochondria, alter host mitochondrial dynamics and β-oxidation function, and interfere with mitochondrial antiviral signaling to promote viral replication [13, 14]. However, it remains unclear whether cellular LDs and mitochondrial homeostasis are impacted by BVDV infection, which viral proteins are involved in the infection process, and the importance of these processes for understanding the pathophysiology of BVDV infection.

This study reveals that BVDV infection promotes intracellular accumulation of LDs, which are subsequently mobilized by the virus for lipolysis. By increasing contact between LDs and mitochondria, lipolysis-dependent FFAs are accelerated and transferred to mitochondria for oxidation, thereby promoting viral replication. We also found that BVDV Core protein targets the surface of LDs, increasing and recruiting FASN and ATGL to promote LD mobilization. At the same time, Core proteins interact with mitochondria, linking mitochondria to LDs and providing an opportunity to release FAs for more efficient FAO. Our findings contribute to elucidating the pathogenetic mechanism of BVDV infection and exploring targets for medical products to control BVDV transmission.

Results

BVDV upregulates LD biogenesis in favor of viral replication

To investigate the role of lipid droplets (LDs) in the BVDV life cycle, we examined the abundance and morphology of these organelles in BVDV-infected bovine cells by immunofluorescence analysis. In this study, BODIPY 493/503, a hydrophobic dye, was used to visualize LDs [15]. We also used an anti-dsRNA antibody to detect BVDV infection. At 12 hours post infection (hpi), BVDV caused an upregulation of LDs in Madin-Darby Bovine Kidney (MDBK) cells and bovine endometrial epithelial cells (BEECs) (Fig. 1A). To further define the dynamics of LD induction following BVDV infection, we set up a time-course analysis. BODIPY staining revealed significant changes in both number and area of LDs in a time-dependent manner during BVDV infection in MDBK cells (Figs. 1B, 1C). Lipid content analysis showed that LDs and their major constituents, triacylglycerols (TAGs) and total cholesterol (TC), were continuously elevated up to 18 hours post infection (hpi) but decreased at 24 hpi (Fig. 1D). In addition, perilipin 2 (PLIN2), a well-known surface marker that maintains LD stability [16], was upregulated and localized around LDs displaying typical doughnut-like circular structures upon infection (Fig. 1E). The mRNA levels of PLIN2 and PLIN3 were also significantly upregulated by BVDV (Fig. 1F). Furthermore, we tested whether MDBK cells and BEECs treated with oleic acid (OA) could further induce LDs. As expected, the number and area of LDs were increased in both MDBK cells (Figs. 1G, 1H) and BEECs (S1A Fig) supplemented with 200 μM oleic acid for 12 h compared to the BSA vehicle. In the early stage of the BVDV life cycle (12 hpi), BVDV was able to further upregulate cellular LD levels in OA-treated bovine cells (Figs. 1G, 1H, S1A Fig).

LDs may exert antiviral or proviral effects at different stages of viral infection [17]. We therefore investigated the role of LDs in the BVDV life cycle. MDBK cells were pretreated with 200 μM OA for 12 hours, followed by infection with BVDV at a multiplicity of infection (MOI) of 0.1, 1, and 5. At 24 hpi, qRT-PCR results showed that intracellular BVDV RNA level was increased by OA except for MOI = 0.1 (Fig. 1I). This increase in viral load suggests that enhanced LD accumulation exerts a proviral replication effect. Together, these data indicate that BVDV modulates cellular lipid homeostasis and LD formation throughout its life cycle, and that increased cellular LDs promote BVDV replication.

BVDV promotes LD biogenesis by stimulating de novo lipogenesis

We then investigated the mechanism by which BVDV infection causes intracellular LDs accumulation. In a serum-free maintenance medium, BVDV induced LD formation (Fig. 2A), suggesting that virally driven LD induction is associated with de novo lipogenesis (DNL). Consistently, the mRNA levels of lipogenic genes *Acly, Acc1, Fasn*, and *Scd1* were upregulated by BVDV (Fig. 2B).

To further investigate the contribution of DNL to LD biogenesis, we assessed LDs by confocal microscopy at 12 hpi using two pharmacological inhibitors: Orlistat, to inhibit the activity of the DNL rate-limiting enzyme FASN [18]; and Torin 1, to inhibit mTOR complex 1 (mTORC1) activity and subsequent SREBP-1C cleavage [19]. Both inhibitors significantly reduced BVDV-induced LDs to basal levels without

affecting cell viability, demonstrating that BVDV-mediated LD biogenesis relies on the DNL pathway (Fig. 2C). qRT-PCR results showed Orlistat or Torin 1 treatment inhibited BVDV replication in a dose-dependent manner at 24 hpi (Fig. 2D). Inhibition of FASN eliminates the production of end-product palmitate and leads to aggregation of earlier pathway intermediates malonyl-CoA [20]. To validate the specificity of these inhibitors, we investigated whether adding exogenous palmitate would restore BVDV replication. Compared to the BSA vehicle, adding BSA-conjugated palmitic acid (PA-BSA) fully reversed the antiviral effects of Orlistat in a dose-dependent manner (Fig. 2D). Taken together, these results indicate that FASN-mediated lipogenesis is important for LD formation and BVDV replication.

BVDV increases exogenous fatty acid uptake

In addition to enhancing de novo FA synthesis, viruses also require the uptake of FAs [21]. Given that PA-BSA fully restores BVDV replication in the FASN-inhibited state, fluorescent FA uptake experiments using the green fluorescent FA analogue BODIPY 500/510 were performed to determine the contribution of exogenous lipids to increasing cellular lipid content [22]. In this paradigm, mock or BVDV-infected MDBK cells were maintained in serum-free medium, making the green FAs were the only exogenous FAs available. MDBK cells were incubated with BODIPY 500/510 for 30 minutes and then uptake was quantified (Fig. 2E). Immunofluorescence analysis of BVDV-infected cells revealed that BODIPY 500/510 aggregated in the cytoplasm into rounded bright structures, and the total fluorescence intensity of intracellular green FAs was significantly increased compared to the mock (Figs. 2F, 2G). Fatty acid uptake and transport require a series of enzymes such as FATP, FABP4, and CD36 [23]. Our results revealed that *FATP* and *FABP4* mRNA levels were significantly increased in BVDV-infected cells, while *CD36* mRNA was significantly reduced compared with mock-infected cells (Fig. 2H).

DGAT is necessary for LD biogenesis during BVDV infection

Diacylglycerol acyltransferase (DGAT) enzymes are responsible for the final step in TAG synthesis, esterifying diacylglycerol (DAG) to TAG, which is then packaged into LDs. Esterification mediated by DGATs is utilized by many viruses to promote viral replication [24, 25]. To further investigate the role of these two enzyme isozymes on LD formation during BVDV infection, virus-infected cells were treated with DGATs pharmacological inhibitors (DGATi). At 12 hpi, MDBK cells treated with DGAT1 inhibitor PF-04620110 harbor scarce LDs, whereas the DGAT2 inhibitor PF-006424439 only partially blocked LD biogenesis without affecting the cell viability. Combined inhibition of DGAT1 and DGAT2 prevents BVDV-induced LD formation to the same extent as DGAT1 inhibition alone (Fig. 2I). Moreover, BVDV infection upregulated *DGAT1* and *DGAT2* mRNA levels (Fig. 2J). Finally, we investigated the effect of DGATi on BVDV replication. Compared to the DMSO vehicle, both DGATi inhibitors significantly reduced BVDV replication in a dose-dependent manner at 24 hpi, especially for DGAT1 (Fig. 2K). Collectively, these data demonstrate that the block of DGAT enzymatic activity disrupts the biogenesis of LDs, thereby disrupting the BVDV replication.

BVDV mobilizes LDs by promoting lipolysis rather than lipophagy

Free fatty acids can be released from LDs for utilization by downstream metabolic pathways, including lipolysis and lipophagy [6]. As autophagy plays a proviral role in a diverse range of *flaviviral* infections [26, 27], cells were treated with bafilomycin A1 (BafA), an inhibitor of V-ATPase and lysosomal acidification, to investigate the effects of BVDV on autophagy via immunoblots. Compared to mock infection, BVDV infection leads to the simultaneous accumulation of the autophagosome marker LC3II and the autophagy substrate p62 under the DMSO vehicle at 12 hpi (Fig. 3A). Autophagic flux was investigated by the standard BafA inhibition assay as per guidelines [28]. As expected, treatment with BafA to block autophagic degradation induced further accumulation of LC3II and p62. After treatment with BafA, the increase in Western blot density of LC3-II was significantly lower in the BVDV-infected group than in the mock group, indicating a decrease in net autophagic flux (Fig. 3A). These results suggest that BVDV is unlikely to mobilize LDs by promoting lipophagy in the early stages of infection.

To further determine which lipolytic pathway is activated during BVDV infection, we performed an OA pulse-chase experiment (Fig. 3B). In this paradigm, MDBK cells were pulsed with 200 μM OA for 12 h to induce LDs and were subsequently treated with DGATi to suppress new LD biogenesis. Cells were then infected with BVDV, with or without various lipolytic inhibitors, and the LD number was assessed by confocal microscopy. The immunofluorescence results demonstrated that, in comparison with the MOCK group, BVDV infection resulted in a sustained reduction in the number of LDs. However, this did not rescue the persistent reduction in LDs during BVDV infection (Figs. 3C, 3D). These observations argue against lipophagy being responsible for enhanced LD turnover at the early stages of BVDV infection. The next step was to investigate if lipolysis was responsible for the turnover of LDs. To this end, ATGL and HSL were pharmacologically inhibited using Atglistatin and CAY10499 [29]. In contrast, we found that Atglistatin and CAY10499 significantly reversed the reduction in LDs caused by BVDV infection (Figs. 3C, 3D), suggesting that BVDV selectively relies on lipolysis to release FAs from LDs. In addition, higher protein and mRNA levels of adipocyte triacylglycerol lipase (ATGL) and hormone-sensitive lipase (HSL) were observed in BVDV-infected cells compared to uninfected cells, whereas the protein level of lysosomal acid lipase (LAL) did not change significantly (Figs. 3E, 3F). These results correlated well with a greater dose-dependent reduction in BVDV replication at 24 hpi when cells were treated with non-toxic concentrations of Atglistatin and CAY10499, but not BafA (Fig. 3G).

Given that the increased LDs induced by OA have a proviral effect (Fig. 1I), we wanted to further study whether inhibiting lipolytic mobilization of pre-existing LDs would affect the proviral effects of OA. Surprisingly, the effect of OA in promoting BVDV replication was completely reversed by Atglistatin, which inhibits the further lipolysis of the LDs after treatment with OA (Fig. 3H). Cellular FFA levels were also significantly reduced when cells were treated with CAY10499 and Atglistatin (Fig. 3I). In summary, our data demonstrate that BVDV relies on the upregulation of ATGL and HSL to promote lipolysis for viral replication.

BVDV enhances the interaction between neutral lipase and LDs instead of increasing LD turnover in lysosomes

Lipolysis and lipophagy are mediated by different lipases (Fig. 4A). Lipophagy, the delivery of LDs to autolysosomes or lysosomes, is mediated by LAL [30]. Lipolysis, the sequential cleavage of triacylglycerols stored in LDs by lipases recruited to the LDs surface, is mediated by neutral lipases such as ATGL and HSL [31].

We first utilized confocal microscopy to rule out the relationship between LD and lipophagy. In mock-infected cells, LDs and lysosomes scattered in the cytoplasm were well separated, with few LDs in contact with or captured by the lysosomal lumen (Fig. 4B). Interestingly, BVDV infection barely alters the association between LDs and lysosomes compared to mock infection (Fig. 4B). We quantified the colocalization of LDs and lysosomes using Pearson's and Mander's correlation coefficients (PCC, MCC). No significant differences between mock and BVDV-infected groups indicate that even if LDs can be engulfed into autophagosomes, they cannot be further delivered to lysosomes for degradation (Fig. 4C).

We then investigated the relationship between LDs and lipolysis-associated neutral lipase by confocal microscopy. ATGL, the first enzyme in the lipolysis pathway, displayed a diffuse cytoplasmic signal and was away from BODIPY-positive structures in mock-infected cells. In BVDV-infected cells, ATGL localized around LDs and showed doughnut-like circular structures (Fig. 4D). HSL, the only diacylglycerol lipase involved in lipolysis, follows a similar distribution pattern to ATGL in the context of BVDV infection (S3A Fig). Quantitative analysis showed that BVDV caused a significant increase in PCC and MCC for both enzymes with co-localization with LDs (Fig. 4E, S3B Fig). Consistent with our OA pulse-chase results, these findings provide compelling evidence that BVDV does not exploit lipophagy but rather lipolysis to facilitate LD mobilization in the early stages of infection.

Regulation of lipid metabolism to beta-oxidative pathways is critical for BVDV replication

We found that the key steps of lipid metabolism including de novo lipogenesis, lipid uptake, TAG synthesis, and lipolysis, are critical for viral proliferation (Fig. 5A). We then investigated whether the antiviral activity of each compound that inhibits these metabolic steps affected the viral life cycle in a single round of BVDV replication. As indicated in the legend, three conditions were tested: (1) single treatment 2 h before BVDV infection, with compound removed before infection; (2) dosage at 1 hpi until 12 hpi; (3) dosage at 6 hpi until 12 hpi (Fig. 5B). Our results showed that Orlistat, PF-04620110, and CAY10499 did not affect the entry stage but significantly inhibited BVDV replication in the post-entry stage (Fig. 5C). To further determine whether the antiviral effects of the three inhibitors could be overcome by adding exogenous FAs in multiple rounds of infection, MDBK cells were mock-infected or infected with BVDV at a MOI of 1. After incubating, cells were treated with each pharmacological inhibitor as above for another 24 h to allow multiple cycles of infection, and simultaneously treated with FA-free BSA vehicle alone or BSA-conjugated palmitic acid (PA-BSA) to specifically rescue the

phenotype. Compared to the BSA vehicle, which did not affect viral load, PA-BSA completely reversed intracellular BVDV RNA levels at 24 hpi (Fig. 5D). Viral supernatants were collected 24 hours after treatment with various inhibitors and then diluted 10-fold and used to infect MDBK cells in 96-well plates for viral titer assays. PA-BSA also completely reversed the inhibitory effect of the inhibitor on extracellular viral titers (Fig. 5E).

The cellular FA pool has been co-opted by diverse viruses for a variety of purposes, including modification of viral proteins such as palmitoylation, or the provision of substrates for energy via fatty acid oxidation (FAO) [7]. We then preliminarily identified the pathways of FA utilization by BVDV using pharmacological inhibitors. To assess the contribution of palmitoylation to BVDV replication, MDBK cells were infected in the presence of vehicle or the palmitate analogue 2-bromopalmitate (2-BP), an inhibitor of palmitoyl acyltransferases [32], and the infectivity and replication of BVDV was determined. Compared to DMSO vehicle, 2-BP did not affect BVDV replication at 24 hpi and had no effect on cell viability (Figs. 5D, 5E), indicating that palmitoylation does not affect the early stages of the BVDV life cycle. Given that ATGL selectively channels the liberated FAs to oxidative pathways [33], we next tested the role of FAO in BVDV replication by using etomoxir, a compound that targets carnitine palmitoyltransferase 1A (CPT1A), preventing the transport of FFAs into the mitochondria [34]. Interestingly, Immunofluorescence analysis showed that etomoxir caused further LD accumulation in BVDV-infected cells without affecting the cell viability (Figs. 5F, 5G). Treatment with etomoxir significantly reduced intracellular BVDV RNA in a way that could not be complemented by replenishing PA-BSA (Figs. 5D, 5E), highlighting the critical role of FAO in the viral life cycle. In summary, our data demonstrate that BVDV induces both lipogenesis and lipolysis, and cellular FAs are transferred into mitochondria to be utilized to facilitate BVDV replication.

BVDV promotes the proximity of LDs to the mitochondrial network and enhances fatty acid oxidation

As dynamic organelles, metabolic crosstalk between mitochondria and LDs via membrane contact sites (MCSs) is well documented in lipid oxidation [35]. Since HCV and DENV target both mitochondria and LDs to create a favorable environment for their proliferation [11, 14], we further investigated the effects of BVDV infection on mitochondria-LD contact and FA transfer to better define the cross-talk between mitochondria and LDs. MDBK cells were treated with OA to expand LDs and the association of mitochondria with LDs was examined using confocal microscopy. Mitochondria were labeled with TOMM20 and LDs with BODIPY 493/503. In mock-infected cells, LDs and mitochondria followed different distribution patterns, with cells exhibiting limited contact between these two organelles (Fig. 6A). In contrast, BVDV-infected cells presented discrete foci where BODIPY structures were in close proximity to TOMM20 structures. Despite the colocalization of LDs and mitochondria being only partial, BVDV infection significantly increased the PCC and MCC in comparison to the mock (Fig. 6B).

Both viral hijacking and excess lipid accumulation promote mitochondrial dysfunction [36, 37]. Therefore, the impact of BVDV infection on mitochondrial homeostasis was studied. Confocal microscopy showed

that mitochondria displayed a round, fragmented morphology as in Fig. 6A and detached from the networks in BVDV-infected cells, as obtained by 2D tubular mitochondrial network analysis at 12 hpi (Fig. 6C) [38]. In comparison, mock-infected MDBK cells displayed a normal mitochondrial network (Fig. 6C). Consistent with the abnormal mitochondrial network, fluorescence microscopy with the mitochondrial membrane potential sensitive dye JC-1 showed a marked increase in green monomers in BVDV-infected cells, indicating mitochondrial depolarization, whereas mock-infected cells displayed predominantly red aggregates, consistent with normal mitochondrial membrane potential (Fig S4). We next investigated the status of mitochondrial biogenesis during BVDV infection. qRT-PCR analysis showed that the transcript levels of biogenesis-related transcriptional activators and cofactors (PPAR-A, PGC1-A, and TFAM) were upregulated in BVDV-infected cells at 12 hpi due to BVDV (Fig. 6D) [40]. Meanwhile, BVDV upregulated the mRNA levels of FAO-related genes [41]. CPT1 and CPT2, which are responsible for the carnitine cycle, as well as Acyl-CoA dehydrogenases (e.g., VLCAD, MCAD, and SCAD) were also upregulated in response to BVDV (Fig. 6E). In summary, by co-opting mitochondrial biogenesis, BVDV could sustain proper mitochondrial FAO function in the context of mitochondrial dysfunction thereby completing its life cycle. In conclusion, BVDV promotes LD-mitochondrial interactions and facilitates mitochondrial biogenesis and FAO function.

BVDV accelerates the transfer of FAs from LDs to mitochondria

Given that BVDV infection increases LD-mitochondrial interactions and upregulates the expression of FAO-related genes, we used a pulse-chase assay with the saturated fluorescent FA analogue BODIPY 558/568 C12 (Red C12) to investigate whether BVDV plays a role in the translocation of FAs (Fig. 7A). At the beginning of the chase period (t = 0 h), bright Red C12 dots in both BVDV- and mock-infected cells co-localized with BODIPY 493/503 (Fig. 7B).

In mock-infected cells, almost all Red C12 signals were retained in LDs throughout the chase period (t = 12 h) (Fig. 7C). In contrast, BVDV-infected cells showed a dramatic loss of Red C12 signal from LDs, with a marked redistribution of signal into mitochondria, resulting in almost complete overlapping of Red C12 with TOMM20. The ATGL-specific inhibitor Atglistatin significantly blocked the transport of Red C12 from LDs to mitochondria induced by BVDV, indicating that lipolysis plays an important role in directing fatty acids towards oxidation.

AICAR, a pharmacological activator of fatty acid beta-oxidation [42], was able to further promote FA transfer from LDs to the mitochondria in BVDV-infected cells without affecting the cell viability (Fig. 7C). Quantitative results of PCC confirmed these findings (Fig. 7D).

Moreover, BVDV caused a progressive decrease in total fluorescence intensity of intracellular Red C12 at 12 hpi, which was reverted by Atglistatin and further boosted by AICAR (Fig. 7E). FAs are transferred from LDs to mitochondria for ATP production. We found that Atglistatin decreased ATP levels compared to those in BVDV-infected cells, whereas AICAR increased ATP levels (Fig. 7F). Finally, AICAR significantly promoted BVDV replication in a dose-dependent manner at 24 hpi (Fig. 7G). In conclusion,

these findings indicate that BVDV promotes mitochondrial-LD interactions and facilitates lipolysis-dependent LD-to-mitochondria FAs transport for ATP production.

BVDV Core protein targets LDs to promote the mobilization of LDs

Given that the Core proteins of both HCV and DENV can target LDs [10, 11], we investigated whether the BVDV Core protein has a similar function. We first examined the colocalization of Red C12-labelled LDs with EGFP-tagged Core under steady state or during LD biogenesis induced by OA treatment for 12 h using confocal microscopy. The empty vector fluorescence was widely distributed throughout the cell and did not co-localize with LDs in either state. Whereas in a steady state, EGFP-Core was punctate and partially co-localized with LDs (Fig. 8A), upon OA treatment, EGFP-Core was remarkably targeted to LDs (Fig. 8B). To better understand the LD targeting mechanism of the Core protein, we used the HeliQuest tool to identify amphipathic helices of the BVDV Core protein [43]. The BVDV Core protein is a 102 amino acid-long peptide containing the first amphipathic helix (AH1), ranging from residues 38 to 55, and the second amphipathic helix (AH2), ranging from residues 79 to 96 (Fig. 8C). The secondary structure predictor PSIPRED and RoseTTAFold protein structure prediction also support the hypothesis of the presence of an amphipathic helix (AH2) at the C-terminus of the Core protein (Fig S5A and S5B). We next expressed EGFP-tagged Core at the C-terminus (Core-eGFP) and found that Core-eGFP did not localize to lipid droplets (LDs) as distinctly as eGFP-Core, suggesting that AH2 may play a crucial role in the localization of the Core protein to LDs (Fig. 8D). In addition, the co-localization pattern of EGFP-tagged Core with LDs, which we labeled with Nile Red [44], was consistent with the above results (Fig S5C and 5D).

We observed that Core protein transient expression led to a significant induction of LDs relative to empty vector in both steady state and OA-treated cells, so we hypothesized that the Core protein may play a direct role in the biogenesis and degradation of LDs. We next used qRT-PCR to determine the mechanism by which Core influences LD abundance. Consistent with observations in BVDV-infected cells, Core overexpression significantly upregulated the RNA levels of lipogenic genes (*ACLY, ACC1, and FASN*) and esterification-related genes (*DGAT1*, *DGAT2*), while Core expression did not affect the RNA level of FA uptake gene (*CD36*, *FATP*) (Fig. 8E), suggesting that BVDV increases de novo lipogenesis through Core proteins and that other viral proteins regulate FA uptake. Overexpression of Core also increased levels of lipolysis-related genes (*ATGL*, *HSL*, and *MGL*) and inhibited autophagy by decreasing LC3II and increasing p62 protein levels (Fig. 8E and Fig S5E), suggesting that BVDV promotes lipolysis rather than lipophagy through its Core protein. Finally, we investigated the possibility that the Core protein regulates de novo lipogenesis and lipolysis by interacting with key enzymes. To this end, EGFP-Core was expressed in bovine cells, and protein interactions were examined by immunoprecipitation. We found that Core protein specifically interacted with endogenous FASN and ATGL compared to the empty vector, while OA treatment further increased their interaction with Core protein (Fig. 8F). Furthermore, the Core protein

increased the interaction with the mitochondrial outer membrane protein TOMM20 compared to EGFP empty vector (S5F Fig).

Compared to vector-transfected cells, Core protein expression not only increased co-localization between Core and mitochondria, but also between Core and LDs, thereby bringing mitochondria and LDs into proximity (Fig. 9A). Moreover, the transfer rate of Red C12 from LDs to mitochondria was significantly higher in EGFP-Core expressing cells compared to vector-transfected cells (Fig. 9B).

To further clarify the functional significance of Core-mediated interactions with lipid metabolic enzymes, we investigated whether Core facilitates lipolysis by recruiting ATGL to lipid droplets (LDs), given that free fatty acids released by ATGL-mediated lipolysis are preferentially directed toward fatty acid oxidation (FAO). To this end, we co-transfected cells with p-EGFP-Core and pCMV-PLIN2-FLAG to confirm LD surface localization, and with p-EGFP-Core and pCMV-ATGL-HA to assess ATGL recruitment. The results showed that the surface of Red C12 lipid droplets transfected with empty vectors was enveloped by PLIN2, whereas Core was significantly localized to the surface of Red C12 lipid droplets compared to empty vectors, forming a colocalized ring-like structure with PLIN2 on the lipid droplet surface, suggesting that Core is indeed localized to the surface of lipid droplets and follows the same distribution pattern as PLIN2 (Fig. 10A). In cells transfected with the empty vector, the neutral lipase ATGL was scattered throughout the cytoplasm and showed almost no colocalization with Red C12 lipid droplets (Fig. 10B). In contrast, while Core is directed to the surface of lipid droplets, it also recruits ATGL to the surface of lipid droplets, where Core and ATGL together form a crescent-shaped structure (shown as white pixels in the figure) (Fig. 10B), confirming that Core can recruit ATGL to the surface of lipid droplets to release fatty acids, thereby accelerating the LD-mitochondrial transfer of lipids.

In summary, our data suggest that the BVDV Core protein targets the surface of lipid droplets, where it recruits key enzymes involved in lipid metabolism: fatty acid synthase (FASN) and adipose triglyceride lipase (ATGL). The Core protein also interacts with mitochondria, thereby linking them to LDs and increasing the efficiency of fatty acid oxidation (FAO).

Discussion

Lipid droplets (LDs) are closely associated with *flaviviral* infection, but little is known about how BVDV utilizes LDs. In this study, we revealed novel mechanisms by which BVDV targets LDs to reprogram cellular metabolism for viral replication: (i) BVDV promotes the accumulation of cellular LDs by enhancing de novo lipogenesis, accelerating exogenous fatty acid uptake, and increasing esterification of FAs; (ii) BVDV promotes lipolysis to release FFAs and increase the cellular FAs pool to promote replication; (iii) BVDV promotes LD-mitochondrial interaction and accelerates FAs transfer to mitochondria for FAO; and (iv) BVDV Core protein targets the surface of LDs, increasing and recruiting FASN and ATGL to promote LD mobilization.

LDs are highly dynamic storage organelles at the center of lipid and energy homeostasis [45]. In addition to a major role in energy storage, LDs are also important cellular hubs that traffic proteins and lipids

between organelles, regulate ER stress, and contribute to viral infections [5, 7]. Previous studies have shown that several RNA viruses enhance lipid droplet formation in the early stages of infection and block lipid biosynthesis inhibiting viral replication [46, 47]. At the same time, other viruses utilize lipolysis or lipophagy to break down LDs in the mid-stage of infection to promote viral replication [48, 49]. Our study showed that BVDV causes an early LD formation and late breakdown during its life cycle. This dynamic change manipulated by BVDV may serve as a common feature of RNA viruses, indicating that LDs play different roles at different stages of infection. It is therefore necessary to determine whether the biogenesis of LDs is beneficial for BVDV replication. Our results suggest that the accumulation of LDs induced by treatment with OA plays a role in promoting viral replication during BVDV infection. The size of LDs also varies with lipid accumulation, and these heterogeneities in size may result in different LD populations performing distinct functions [50]. In contrast to the significant increase in number and area, the mean diameter of LDs remained at approximately 1.4 μm after infection. LD size depends on the net result of nascent LD biogenesis and mature LD degradation. To better investigate the effect of BVDV infection on LD dynamics, subsequent experiments could employ GPAT4, a membrane marker for nascent LDs [51], and HSD17B11, a marker for mature LDs [52], to validate changes in different LD populations.

The increased LD number induced by BVDV could be due to increased intracellular FA production and esterification, decreased lipid hydrolysis from LDs, or a combination of the above two situations. As a barrier to maintaining LD homeostasis, PLIN2 (also known as ADRP) and PLIN3 (also known as TIP47) were recruited to the surface of LDs during their biogenesis [16]. With LD maturation, PLIN3 is progressively displaced and remains stable in the cytoplasm [53]. The mRNA levels of these PLINs in this study increased significantly with infection, especially that of *PLIN3*, suggesting that BVDV likely promotes overall LD biogenesis.

Triacylglycerols required for LD biogenesis are primarily derived from exogenously circulating lipids and endogenously synthesized FAs. Through DNL, FAs are synthesized from acetyl-CoA generated from glucose, glutamine, or acetate. This acetyl-CoA is then synthesized into palmitate and further elongated and desaturated through a series of enzymatic reactions [54]. Together with FAs taken up from the environment, they form a complex pool of substrates for the synthesis of FA-containing lipids. DNL induced by viral infection can reduce viral dependence on externally supplied lipids [55]. We first assessed the DNL capacity of BVDV laterally by excluding exogenous lipid availability in FA-free medium. The mRNA levels of the major lipogenic genes were all increased significantly by BVDV infection, suggesting that BVDV fully activates the DNL pathway at the transcriptional level. Studies have shown that viruses depend on the selected pathways, such as EGFR, TGF-β, and SREBP-1 pathways, to promote LD production [56, 57]. Our data suggest that BVDV infection activates certain relevant transcription factors, and subsequent experiments could employ the luciferase assay to further investigate the transcriptional mechanisms responsible for BVDV induced lipogenesis.

It is important to note that the FASN inhibitor Orlistat may cause side effects such as the accumulation of malonyl-CoA or acting on other unidentified targets. Accumulation of malonyl-CoA can further lead to

protein malonylation or cytotoxicity [58]. We ruled out these non-specific effects by back-complementation assays, but the ability of PA-BSA to completely reverse the antiviral effects of Orlistat suggests that BVDV can use exogenous lipids. Metabolic flexibility allows cells to compensate for disrupted lipid homeostasis by switching to the uptake of exogenous FAs in states that limit lipid synthesis, such as hypoxia or nutrient deprivation [59]. We confirmed the increase in exogenous lipid uptake by BODIPY 500/510. However, changes in the expression of several enzymes responsible for FA uptake were not consistent. These observations suggest that antiviral therapy using FASN inhibitors needs to be considered in conjunction with reducing the availability of exogenous FA and investigating the molecular mechanisms responsible for lipid uptake.

Diacylglycerol acyltransferase enzymes (DGATs) mediate the final committed step in TAG synthesis. DGAT1 is completely ER-resident, whereas DGAT2 localizes to both the ER and around LDs. These differences in location may represent distinct functions in LD biogenesis. DGAT1 is mainly responsible for incorporating exogenous FAs into TAG or re-esterifying FAs after lipolysis, whereas DGAT2 is thought to play a major role in esterifying de novo synthesized FAs [60]. Considering the efficiency of DGAT1 inhibition alone and the importance of DGAT1 for preventing mitochondrial dysregulation and ER stress under lipolytic conditions [37], we used only PF-04620110 to inhibit new LD biogenesis in subsequent pulse-chase experiments to explore the possibility of LD degradation.

Considering the kinetic changes in LDs during BVDV infection with a sustained increase followed by a decrease at 24 hpi, we hypothesize that LD degradation occurs concurrently with LD synthesis during the early stages of BVDV infection, but is masked by the intense LD biogenesis. Existing studies on *flavivirus* initially led us to explore the role of lipophagy in the mobilization of LDs [26, 27]. However, either an increase in autophagosome formation or a decrease in autophagosome degradation increased LC3II levels, but in our case this increase was accompanied by an accumulation of p62, suggesting that autophagic degradation was blocked in the context of BVDV infection. Consistent with our LC3 II turnover results, OA pulse-chase experiments and unchanged LAL protein levels together exclude the contribution of lipophagy to the mobilization of LDs by BVDV. More recent studies have demonstrated that lipolysis acts as an upstream regulator of lipophagy in hepatocytes, facilitating the breakdown of larger LDs into smaller LDs [61]. Our experiments confirmed that lipolysis degraded LDs in a state of lipophagy inhibition, but the HSL-specific inhibitor CAY10499 was more efficient in limiting LD production and viral replication compared to Atglistatin. ATGL is a well-characterized major TAG lipase in adipose tissue and heart, but additional TAG lipases in non-adipocyte tissue function redundantly to ATGL and compensate for its inhibition [62]. HSL is the only diacylglycerol lipase that cleaves diacylglycerol to monoacylglycerol and free FAs. Although confocal results showed that BVDV increased the interaction between LD and these two neutral lipases at the same time, inhibition of the enzymatic activity of HSL had a more potential effect on prohibiting BVDV replication. CAY10499 causes aggregation of LDs with concomitant impairment of viral replication, but this is distinct from the LD-dependent enhancement of BVDV replication by OA. Meanwhile, CAY10499 was able to completely reverse the effect of OA in promoting BVDV replication. These data suggest that increasing the number of LDs does not always support BVDV replication, as FAs released from lipolysis are critical for viral replication.

Studies have shown that SARS-CoV-2 and DENV promote replication via cellular beta-oxidation [49, 63], whereas HCV-induced lipid oxidation is detrimental to the viral life cycle and might be part of a host metabolic antiviral response [34]. We then used etomoxir to confirm the effect of fatty acid oxidation on viral replication. Etomoxir also causes aggregation of LDs with concomitant impairment of viral replication, and this inhibition could not be fully rescued by PA-BSA. It is reasonable to speculate that the liberated FAs must be transferred to the mitochondria to exert their proviral effect.

Although the biochemical basis of FA import into mitochondria has been extensively studied, how FAs are transferred from LDs to mitochondria to drive FA oxidation is still not fully understood. According to current models, FAs transfer most likely occurs at mitochondria-LD MCSs, where the membranes of the two opposing organelles are in close proximity (typically 10–30 nm) [64]. This spatial proximity would reduce the accumulation of cytosolic-free FAs, preventing lipotoxicity and/or aberrant lipid signaling. Mitochondrial-LD interactions induced by BVDV infection are thus hypothesized to provide a bridge for the transfer of FAs to mitochondria, but direct transfer remains difficult to demonstrate. To enable visualization of FA transfer from LDs to mitochondria, we utilized a widely-characterized fluorescent FA analog-based pulse-chase assay by using BODIPY-C12 (Red C12) and adapted it to specific details [9]. It should be noted that Red C12 has different biophysical properties than endogenous FAs, thus affecting their transport and metabolism and producing non-specific results [65]. Therefore, the FA transport result should be further verified in the subsequent experiments by using isotope-labeled FAs.

Mitochondrial homeostasis is critical for FAO function. In this study, we observed a considerable upregulation in the mRNA levels of enzymes responsible for both the carnitine cycle and dehydrogenation in response to an increase in the cellular fatty acid pools within BVDV-infected cells. Excessive fatty acid oxidation during viral infection may lead to mitochondrial dysfunction [37]. Our results demonstrated that BVDV infection deficiency resulted in abnormal mitochondrial morphology and dissociation of the mitochondrial network. Thus, the BVDV-induced increase in transcription factors associated with mitochondrial biogenesis could compensate for this impairment.

The association between +ssRNA viral proteins and LDs is particularly strong: HCV and DENV capsid proteins co-localize with LDs [10, 11]; Poliovirus protein 2BC is cleaved into 2B and 2C and targeted to LDs [29]; and Coronavirus ORF6 protein is targeted to LDs and localizes at the mitochondrial-LD contact site [63]. Viral proteins utilizing amphipathic helices have been identified to target LDs, and depletion of amphipathic helices abolished LD association [66]. In this study, we found that there are two amphipathic helices in the Core protein and that the C-terminal helix may be primarily responsible for direct insertion into the LD lipid monolayer. To determine whether the two amphiphilic helices were required for Core-LD binding, subsequent experiments required the introduction of point mutations at the hydrophobic interface of each helix to disrupt their structure.

Viral proteins can physically interact with the lipogenesis and lipolysis machinery [63]. In our experiments, the BVDV Core protein interacts with FASN, ATGL, and TOMM20. Given that antiviral strategies often focus on directly targeting viral proteins [67], further experiments will require the

construction of truncated mutants and the application of in vitro GST pull-down assays to further confirm the direct interactions between Core and host proteins, laying the groundwork for the development of broad-spectrum antiviral strategies targeting host factors critical for virus replication.

Conclusions

This study reveals that BVDV infection promotes intracellular accumulation of LDs, which are subsequently mobilized by the virus via lipolysis. By increasing contact between LDs and mitochondria, lipolysis-dependent FFAs are rapidly transferred to mitochondria for oxidation, thereby promoting viral replication. The BVDV Core protein targets lipid droplets and recruits FASN and ATGL, thereby promoting the mobilization of LDs. This Core protein also interacts with mitochondria, potentially providing a bridge for the transfer of FAs from LDs to mitochondria. Our findings help elucidate the pathogenic mechanisms of BVDV infection and identify potential targets for therapies aimed at controlling BVDV transmission.

Materials and Methods

Cell culture and virus infection

Madin-Darby bovine kidney (MDBK) cells and bovine endometrial epithelial cells (BEECs) were cultured in Dulbecco's modified Eagle's medium (DMEM) (SH30243.01, Cytiva) supplemented with 1% antibiotic-antimycotic (15140163, Gibco) and 10% fetal bovine serum (FBS) (12303C, Sigma-Aldrich). The cells used in the study tested negative for Mycoplasma spp. The BVDV AV67 strain was obtained from the China Veterinary Culture Collection (Beijing, China) and stored in our laboratory for use in subsequent experiments. MDBK cells and BEECs were mock-infected or infected with BVDV strain AV67 at a multiplicity of infection (MOI) of 0.1, 1, and 5. After 1 h of absorption at 37°C in a 5% CO_2 incubator, the cells were washed three times with PBS to remove unbound virus and then cultured at 37°C in DMEM supplemented with 2% FBS.

Antibodies and reagents

Antibodies against GFP (mouse, HRP-66002), P62 (rabbit, 18420-1-AP), ATGL (rabbit, 55190-1-AP), HSL (rabbit, 17333-1-AP), LAL (rabbit, 12956-1-AP), LAMP1 (rabbit, 21997-1-AP), TOMM20 (rabbit, 11802-1-AP), FASN (rabbit, 10624-2-AP), and β-actin (mouse, 66009-1-Ig) were purchased from Proteintech. Antibodies against LC3 (rabbit, #12741) was obtained from Cell Signaling. Antibody against dsRNA (J2) was obtained from Cell Signaling. HRP-conjugated goat anti-mouse or rabbit IgG were obtained from Proteintech. Alexa Fluor 488/568-conjugated goat anti-mouse or rabbit IgG were purchased from Life Technologies. Anti-eGFP magnetic agarose beads (HY-K0246), Palmitic acid (HY-N0830), and Nile Red (HY-D0718) were obtained from MCE. BODIPY 493/503 (D3922) and BODIPY 558/568 C12 (D3835) were purchased from ThermoFisher Scientific. Oleic acid (O1008) and the DGAT2 inhibitor (PF-006424439) were purchased from Sigma-Aldrich. BODIPY 500/510 (C2055) was purchased from Beyotime. Orlistat (HY-B0218), Torin 1 (HY-13003), PF-04620110 (HY-13009), Bafilomycin A1 (HY-100558), Atglistatin (HY-

15859), CAY10499 (HY-119283), 2-BP (HY-111770), and Etomoxir (HY-50202) were obtained from MCE. AICAR (S1802) was purchased from Selleck.

Cell viability assay

Cell viability was determined using a Cell Counting Kit-8 (C0038, Beyotime). In brief, 5000 cells per well were seeded in a 96-well plate and allowed to grow in the medium overnight. On the second day, the medium was removed and the cells were incubated with a given concentration of the compound for 36 h. At the end of each treatment, the medium was replaced and CCK-8 (10 mL) was added to each well and incubated at 37°C for 2 h. After the cells were incubated for another 2 h, the absorbance was detected at 450 nm. The effects of the compounds on cell viability are shown in S2A Fig.

Quantitative real-time PCR

Total RNA was extracted from mock or BVDV-infected MDBK cells using a total RNA kit (R6834-01, Omega) and cDNA was synthesized using a TransStart one-step gDNA removal and cDNA synthesis supermix kit (AE341-02, TransGen) according to the manufacturer's instructions. GAPDH and β-actin were used as reference genes. Results are presented as fold change compared to matched controls using the $2^{-\Delta\Delta CT}$ method. Primer sequences are shown in Table 1.

Table 1
Primers used in this study.

Gene	Direction	Sequence (5'-3')
PLIN2	F	AGTGAACTTGCCAGGAAGAATG
	R	TTCATCTGTATCATCGTAGCCG
ACLY	F	GTCAACCTCACTCTGGATGGA
	R	TCGTGGTGGAACAGGACATAG
ACC1	F	GGGTGAAAGACTGGGTTGAA
	R	GACAGAGCACGGATGTGATG
FASN	F	TCCCACTGGAACAAGACAAGC
	R	TTTCTTTTGAAGTTGAGGGAGGC
SCD1	F	TCCGACCTAAGAGCCGAGAA
	R	TGGGCAGCACTATTCACCAG
CD36	F	GGTCCTTACACATACAGAGTTCG
	R	ATAGCGAGGGTTCAAAGATGG
FATP	F	GGGGCAGTGTCTCATCTATGG
	R	CCGATGTACTGAACCACCGT
FABP4	F	TGGGATGGAAAATCAACCAC
	R	TGGCTTATGCTCTCTCATAAAC
DGAT1	F	CCACTGGGACCTGAGGTGTC
	R	GCATCACCACACACCAATTCA
DGAT2	F	AATCGCAAGGGCTTTGTGAAAC
	R	CCCCAGGTGTCAGAGGAGAAGA
ATGL	F	CTCTGATGGCGAGAACGTCA
	R	TTGTCTGAGATGCCACCGTC
HSL	F	AGTCCCACCTGAAATCAGTGT
	R	CCAAGTAAGAAGTTGATGGTT
MGL	F	GCAACCAGCTGCTCAACAC
	R	AGCGTCTTGTCCTGGCTCTT
PPAR-A	F	CGGTGTCCACGCATGTGA

Gene	Direction	Sequence (5'-3')
	R	TCAGCCGAATCGTTCTCCTAAA
PGC1-A	F	GTGAAGACCAGCCTCTTTGC
	R	TCACTGCACCACTTGAGTCC
TFAM	F	GGCACATCACAGGTAAAGC
	R	AATTGAGCGACGTATAAGAT
CPT1A	F	CAAAACCATGTTGTACAGCTTCCA
	R	GCTTCCTTCATCAGAGGCTTCA
CPT2	F	TGCCTTCCTTCCTGTCTTGGTATG
	R	GGGTCTGGGTAAACGAGTTGAATTG
VLCAD	F	TTCCATACCCGTCTGTGCTCAAC
	R	GGCAGCATCGTTCACCTCCTC
MCAD	F	CAGACACCCCAGGAGTACAGATTG
	R	TTCCTTGGGCACTCTCACATCTTC
SCAD	F	CTGGACTGTGCTGTGACCTACG
	R	GCCATGTCCGCCAACTTGAAC
BVDV-5'UTR	F	TAGTCGTCAGTGGTTCGACGC
	R	CCTCTGCAGCACCCTATCAG
PLIN3	F	GAGCGGGGTGGACACAGTGC
	R	CAAGGGATGTGGCGAGGCGG
β-actin	F	AAGGACCTCTACGCCAACACG
	R	TTTGCGGTGGACGATGGAG

Virus titration

The MDBK cells were incubated with BVDV at 37°C for 1 h, after which the unbound viruses were washed off and the cells were cultured in supplemented medium. After repeated freezing and thawing twice, the whole-cell culture supernatant was harvested by centrifugation. This was then serially diluted 10-fold to infect MDBK cells in 96-well plates. After incubation at 37°C for 24 h, the cells were fixed with 4% paraformaldehyde for 10 min at room temperature, and an immunofluorescence assay was performed using a mouse anti-dsRNA (J2) antibody and an Alexa Fluor 488-labelled goat anti-mouse IgG secondary antibody to visualise viral infection. Viral titers were measured using the Reed-Muench assay and

expressed as the logarithm of the infectious dose per 0.1 mL of 50% tissue culture infective dose ($TCID_{50}$/0.1 mL).

Western blotting

Cells were lysed on ice for 20 min in radioimmunoprecipitation assay (RIPA) buffer (R0010, Solarbio) supplemented with proteases/phosphatase inhibitor cocktail (#5872, Cell Signaling). Protein samples were subjected to electrophoresis on 8%, 10%, or 15% gradient SDS-PAGE gels, depending on the molecular weight of the protein, and then transferred to a polyvinylidene fluoride membrane (HATF00010, Millipore). After blocking in 5% skimmed milk for 1.5 h at room temperature, membranes were washed three times for 5 min each with PBST and incubated with appropriate primary antibodies overnight at 4°C, followed by HRP-conjugated secondary antibodies for 1.5 h at room temperature. Targeted protein bands were detected using an ECL-enhanced chemiluminescence detection system (Tanon 6200, Shanghai, China). The bands were quantified by densitometry using Fiji software (version 1.50).

Confocal fluorescence microscopy

For immunostaining, cells grown on climbing sheets were washed three times with PBS, fixed with 4% paraformaldehyde for 15 min, and permeabilized with 0.1% Triton X-100 in PBS for 15 min. Cells were blocked with 2% bovine serum albumin in PBST for 60 min. Primary antibodies were incubated in 1% BSA overnight at 4°C, followed by Alexa Fluor-conjugated secondary antibody for 1 h at room temperature. LDs were stained with BODIPY 493/503, BODIPY 558/568 C12, or Nile Red in the dark for 30 min, and nuclei were stained with 4,6-diamidino-2-phenylindole (10236276001, Sigma-Aldrich) for 5 min at room temperature. The coverslips were then mounted onto slides and visualized using a Nikon A1 confocal laser scanning microscope.

Fluorescent fatty acid uptake

For the fatty acid uptake assay, MDBK cells were either mock-infected or BVDV-infected at an MOI of 5. After 1 h of absorption, cells were washed three times with PBS and maintained in fresh phenol red-free DMEM. At 11.5 hpi, cells were washed with PBS and incubated for 30 min at room temperature in the dark in DMEM medium containing 5 μM of the fluorescent fatty acid analogue BODIPY 500/510. At 12 hpi, the cells were fixed with 4% PFA. BODIPY 500/510 uptake was quantified by measuring the intracellular green fluorescence signal by confocal imaging.

Fluorescence fatty acid labeling

The transfer of lipids from LDs to mitochondria was monitored as previously described (9). In brief, BODIPY 558/568 C12 was added to the culture medium of MDBK cells at a final concentration of 2 μM for 8 h before infection, followed by three washes with PBS and virus infection at MOI = 3 for 1 h. After 1 h of absorption, cells were then washed and chased in DMEM supplemented with 1% FBS for 12 h and

then fixed with 4% PFA. TOMM20 antibody was used as a mitochondrial marker for cell staining and visualization by confocal imaging.

Fluorescent image analysis

The fluorescent images used for phenotype quantification were acquired below saturation using identical parameters (i.e. PMT HV, PMT offset, laser power, and magnification) and processed using Fiji software. The “Analyze Particles” macro was used to measure the number and size of LDs in thresholded images, the Pearson’s correlation coefficient and Manders’ colocalization coefficient in two channels were calculated to quantify co-localization using the JACoP plugin in Fiji software. The 2D traces of the tubular mitochondrial network obtained by the Skeletonize 2D/3D plugin of ImageJ. Brightness and contrast were adjusted using identical settings in Adobe Photoshop, and panels were assembled using Adobe Illustrator. The images shown are representative of at least three independent experiments.

Cellular triacylglycerol, total cholesterol, and free fatty acid measurement

Cells treated in different experiments were harvested and washed three times with PBS. Intracellular triacylglycerol, cholesterol, and free fatty acids were measured using the triglyceride assay kit (BC0620, Solarbio), total cholesterol assay kit (BC1980, Solarbio), and Amplex Red Free Fatty Acid Assay Kit (BC0590, Solarbio) according to the manufacturer’s protocols. Results were standardized to the total cellular protein content.

Cellular ATP measurement

ATP was measured using an ATP assay kit (S0026, Beyotime) according to the manufacturer's protocols. Results were standardized to the total cellular protein content.

DNA construction and transfection

The plasmids encoding C-terminus flag tagged BVDV strain AV67 Core proteins were generous gifts from Jing Wang (Zhejiang A&F University). The pEGFP-C1 and pEGFP-N1 vectors were stored in our laboratory. Core-FLAG was used as a template to generate the N-terminus tagged mammalian expression plasmids p-EGFP-Core and the C-terminus tagged expression plasmid p-Core-EGFP. Plasmid DNAs were transfected into bovine endometrial epithelial cells using Lipofectamine 3000 (L3000015, ThermoFisher) according to the manufacturer's instructions. Transfection efficiency was detected by immunofluorescence of the EGFP tag.

Immunoprecipitation

Bovine cells were transfected with the pEGFP-C1 or pEGFP-Core plasmid and cultured at 37°C in 5% CO_2 for 36 h. Next, the cells were collected and lysed in IP lysis buffer (P0013, Beyotime) containing protease inhibitor phenylmethylsulfonyl fluoride (PMSF) (P8340, Solarbio). Lysates were centrifuged at 12,000 g

for 15 min at 4°C. 20% of the supernatant was saved as input for immunoblotting analysis. Meanwhile, 20 μL of anti-eGFP magnetic agarose beads (HY-K0246, MCE) were washed with lysis buffer and added to the remaining protein samples, and incubated overnight at 4°C. Subsequently, the beads were washed three times with PBS and eluted with 2 × SDS loading buffer. Co-immunoprecipitated proteins were analyzed by Western blot.

Statistical analysis

All statistical analyses were performed with GraphPad Prism V9.0 software. For quantitative analyses, data from at least three independent experiments are expressed as means ± SEM to ensure reproducibility. Data were analyzed using a two-tailed Student's *t* test or a one-way analysis of variance (ns, $p > 0.05$; *, $p < 0.05$; **, $p < 0.01$; ***, $p < 0.001$). No data were excluded from the analyses.

Declarations

Ethics approval and consent to participate

Not applicable.

Consent for publication

Not applicable.

Funding

This work was supported by the National Key R&D Program of China (2023YFD1801100), Hainan Province Science and Technology Special Fund of China (ZDYF2024XDNY198), the National Natural Science Foundation of China (32202853), and the 2115 Talent Development Program of China Agricultural University.

Author Contribution

X.X. wrote the manuscript. X.W., Y.L., and Y.Z. conducted data analysis. J.W. and G.Y. conceived and designed the manuscript. All authors have read and approved the manuscript.

Acknowledgement

The authors would like to thank Dr. Xuefei Wang and Dr. Hao Yang for their assistance in preparing the manuscript.

Data Availability

The data will be shared upon request by the readers.

References

1. Harada T, Tautz N, Thiel J (2000) E2-p7 region of the bovine viral diarrhea virus polyprotein: Processing and functional studies. J Virol 74:9498–9506
2. Scharnböck B, Roch F, Richter V, Funke C, Firth L, Obritzhauser W, Baumgartner W, Käsbohrer A, Pinior B (2018) A meta-analysis of bovine viral diarrhoea virus (BVDV) prevalences in the global cattle population. Sci Rep 8:15
3. Kubati G, Hussen J, Kandeel M, Mubarak A, Hemida G (2021) Recent advances on the bovine viral diarrhea virus molecular pathogenesis, immune response, and vaccines development. Front Vet Sci 8:15
4. Ketter E, Randall G (2019) Virus impact on lipids and membranes. Ann Rev Virol 6:319–340
5. Olzmann A, Carvalho P (2019) Dynamics and functions of lipid droplets. Nat Rev Mol Cell Biol 20:137–155
6. Zechner R, Madeo F, Kratky D (2017) Cytosolic lipolysis and lipophagy: two sides of the same coin. Nat Rev Mol Cell Biol 18:671–684
7. Monson A, Trenerry M, Laws L, Mackenzie M, Helbig J (2021) Lipid droplets and lipid mediators in viral infection and immunity. FEMS Microbiol Rev 45:45:20
8. Qu Q, Zeng F, Liu X, Wang J, Deng F (2016) Fatty acid oxidation and carnitine palmitoyltransferase I: emerging therapeutic targets in cancer. Cell Death Dis 7:9
9. Rambold S, Cohen S, Lippincott-Schwartz J (2015) Fatty acid trafficking in starved cells: regulation by lipid droplet lipolysis, autophagy, and mitochondrial fusion dynamics. Dev Cell 33:489–490
10. Bley H, Schöbel A, Herker E (2020) Whole lotta lipids-from HCV RNA replication to the mature viral particle. Int J Mol Sci 21:12
11. Byk A, Gamarnik V (2016) Properties and functions of the dengue virus capsid protein. Ann Rev Virol 3:263–281
12. Shang F, Son H, Shi Y, Qi X, Gao F (2018) Crystal structure of the capsid protein from Zika virus. J Mol Biol 430:948–962
13. Chatel L, Cortese M, Romero I, Bender S, Neufeldtv J, Fischl W et al (2016) Dengue virus perturbs mitochondrial morphodynamics to dampen innate immune responses. Cell Host Microbe 20:342–356
14. Siu Y, Zhou F, Yu K, Zhang L, Wang L, Liang H et al (2016) Hepatitis C virus NS5A protein cooperates with phosphatidylinositol 4-kinase IIIα to induce mitochondrial fragmentation. Sci Rep 6:13
15. Qiu B, Simon C (2016) Bodipy 493/503 staining of neutral lipid droplets for microscopy and quantification by flow cytometry. Bio-protocol ; 6
16. Sztalryd C, Brasaemle L (2017) The perilipin family of lipid droplet proteins: Gatekeepers of intracellular lipolysis. Biochim Biophys Acta Mol Cell Biol Lipids 1862:1221–1232

17. Monson A, Crosse M, Duan M, Chen W, O'shea D, Wakim M et al (2021) Intracellular lipid droplet accumulation occurs early following viral infection and is required for an efficient interferon response. Nat Commun 12:17
18. Chu J, Xing S, Du Y, Duan H, Liu Y, Zhang F et al (2021) Pharmacological inhibition of fatty acid synthesis blocks SARS-CoV-2 replication. Nat Metab 3:1466
19. Hosios M, Wilkinson E, McNamara C, Kalafut C, Torrence E, Asara M et al (2022) Manning, mTORC1 regulates a lysosome-dependent adaptive shift in intracellular lipid species. Nat Metab 4:1792
20. Brining U, Morales F, Kalucka J, Goveia J, Taverna F, Queiroz S et al (2018) Impairment of angiogenesis by fatty acid synthase inhibition involves mTOR malonylation. Cell Metab 28:866
21. Nchoutmboube A, Viktorova G, Scott J, Ford A, Pei T, Watkins A et al (2013) Increased long chain acyl-Coa synthetase activity and fatty acid import is linked to membrane synthesis for development of picornavirus replication organelles. PLoS Pathog 9:20
22. Wang B, Rong X, Duerr A, Hermanson J, Hedde N, Wong S et al (2016) Intestinal phospholipid remodeling is required for dietary-lipid uptake and survival on a high-fat diet. Cell Metab 23:492–504
23. Bazinet P, Layé S (2014) Polyunsaturated fatty acids and their metabolites in brain function and disease. Nat Rev Neurosci 15:771–785
24. Yuan F, Yan P, Cao L, Ye W, Liang H, Tang M et al (2021) SARS-CoV-2 exploits host DGAT and ADRP for efficient replication. Cell Discov 7:13
25. Herker E, Harris C, Hernandez C, Carpentier A, Kaehlcke K, Rosenberg R et al (2010) Efficient hepatitis C virus particle formation requires diacylglycerol acyltransferase-1. Nat Med 16:1295–1298
26. Lan Y, Leur W, Fernando A, Wong H, Kampmann M, Siu L et al (2023) Viral subversion of selective autophagy is critical for biogenesis of virus replication organelles. Nat Commun 14:15
27. Zhang S, Lan Y, Li Y, Lamers M, Fusade M, Klemm E et al (2018) Flaviviruses exploit the lipid droplet protein AUP1 to trigger lipophagy and drive virus production. Cell Host Microbe 23:819
28. Rowland A, Guilherme A, Henriques F, Dimarzio C, Munroe S, Wetoska N et al (2023) De novo lipogenesis fuels adipocyte autophagosome and lysosome membrane dynamics. Nat Commun 14:14
29. Laufman O, Perrino J, Andino R (2019) Viral generated inter-organelle contacts redirect lipid flux for genome replication. Cell 178:275
30. Schulze J, Krueger W, Weller G, Johnson M, Casey A, Schott B et al (2020) Direct lysosome-based autophagy of lipid droplets in hepatocytes. Proc Natl Acad Sci 117:32443–32452
31. Kaushik S, Cuervo M (2015) Degradation of lipid droplet-associated proteins by chaperone-mediated autophagy facilitates lipolysis. Nat Cell Biol 17:759
32. Davda D, Azzouny A, Tom C, Hernandez L, Majmudar D, Kennedy T et al (2013) Profiling targets of the irreversible palmitoylation inhibitor 2-bromopalmitate. ACS Chem Biol 8:1912–1917

33. Sathyanarayan A, Mashek T, Mashek G (2017) ATGL promotes autophagy/lipophagy via SIRT1 to control hepatic lipid droplet catabolism. Cell Rep 19:1–9
34. Levy G, Habib N, Guzzardi A, Kitsberg D, Bomze D, Ezra E et al (2016) Nuclear receptors control pro-viral and antiviral metabolic responses to hepatitis C virus infection. Nat Chem Biol 12:1037
35. Wang R, Fang N, Xiong J, Du J, Cao Y, Ji K (2021) An ESCRT-dependent step in fatty acid transfer from lipid droplets to mitochondria through VPS13D-TSG101 interactions. Nat Commun 12:16
36. Khan M, Syed H, Kim J, Siddiqui A (2015) Mitochondrial dynamics and viral infections: A close nexus. Biochim Biophys Acta-Mol Cell Res 1853:2822–2833
37. Nguyen B, Louie M, Daniele R, Tran Q, Dillin A, Zoncu R et al (2017) DGAT1-dependent Lipid droplet biogenesis protects mitochondrial function during starvation-induced autophagy. Dev Cell 42:9
38. Singh B, Avula K, Sufi A, Parwin N, Das S, Alam F et al (2022) Defective mitochondrial quality control during dengue infection contributes to disease pathogenesis. J Virol 96:29
39. Barbier V, Lang D, Valois S, Rothman L, Medin L (2017) Dengue virus induces mitochondrial elongation through impairment of Drp1-triggered mitochondrial fission. Virology 500:149–160
40. Sato H, Hoshi M, Ikeda F, Fujiyuki T, Yoneda M, Kai C (2021) Downregulation of mitochondrial biogenesis by virus infection triggers antiviral responses by cyclic GMP-AMP synthase. PLoS Pathog 17:24
41. Houten M, Violante S, Ventura V, Wanders A (2016) The biochemistry and physiology of mitochondrial fatty acid β-oxidation and its genetic disorders. Ann Rev Physiol 78:23–44
42. Fernandes O, Zeidler D, Sousa G, Ferreira T, Da T (2018) Anaplerotic role of glucose in the oxidation of endogenous fatty acids during dengue virus infection. mSphere 3:16
43. Gautier R, Douguet D, Antonny B, Drin G (2018) A web server to screen sequences with specific α-helical properties. Bioinformatics 24:2101–2102
44. Escorcia W, Ruter L, Nhan J, Curran P (2018) Quantification of lipid abundance and evaluation of lipid distribution in caenorhabditis elegans by nile red and oil red o staining. J Vis Exp 133:57352
45. Bosch M, Sweet J, Parton G, Pol A (2021) Lipid droplets and the host-pathogen dynamic: FATal attraction. J Cell Biol 220:18
46. Dias G, Soares C, Ferreira C, Sacramento Q, Fintelman N, Temerozo R et al (2020) Lipid droplets fuel SARS-CoV-2 replication and production of inflammatory mediators. PLoS Pathog 16:19
47. Liefhebber P, Hague V, Zhang F, Wakelam O, McLauchlan J (2014) Modulation of triglyceride and cholesterol ester synthesis impairs assembly of infectious hepatitis C virus. J Biol Chem 289:21276–21288
48. Baek B, Kwon J, Sharif M, Lim J, Lee C, Ryu B et al (2022) Therapeutic strategy targeting host lipolysis limits infection by SARS-CoV-2 and influenza A virus. Signal Transduct Target Ther 7:12
49. Heaton S, Randall G (2010) Dengue virus-induced autophagy regulates lipid metabolism. Cell Host Microbe 8:422–432

50. Yang Y, Galea A, Sytnyk V, Crossley M (2012) Controlling the size of lipid droplets: lipid and protein factors. Curr Opin Cell Biol 24:509–516
51. Wilfling F, Wang J, Haas T, Krahmer N, Gould J, Uchida A et al (2013) Triacylglycerol synthesis enzymes mediate lipid droplet growth by relocalizing from the ER to lipid droplets. Dev Cell 24:84–399
52. Song J, Mizrak A, Lee W, Cicconet M, Lai W, Tang C et al (2022) Identification of two pathways mediating protein targeting from ER to lipid droplets. Nat Cell Biol 24:1364
53. Choi M, Ajjaji D, Fleming D, Borbat P, Jenkins L, Moeller E et al (2023) Structural insights into perilipin 3 membrane association in response to diacylglycerol accumulation. Nat Commun 14:16
54. Snaebjornsson T, Janaki S, Schulze A (2020) Greasing the wheels of the cancer machine: the role of lipid metabolism in cancer. Cell Metab 31:62–76
55. Greseth D, Traktman P (2014) De novo fatty acid biosynthesis contributes significantly to establishment of a bioenergetically favorable environment for vaccinia virus infection. PLoS Pathog 10:16
56. Patra T, Sasaki R, Meyer K, Ray B, Ray R (2019) Transforming growth factor β acts as a regulatory molecule for lipogenic pathways among hepatitis C virus genotype-specific infections. J Virol 93:14
57. Wang L, Xie W, Zhang L, Li DF, Yu H, Xiong JZ et al (2018) CVB3 Nonstructural 2A protein modulates SREBP1a signaling via the MEK/ERK pathway. J Virol 92:15
58. Munger J, Bennett D, Parikh A, Feng XJ, McArdle J, Rabitz A et al (2008) Systems-level metabolic flux profiling identifies fatty acid synthesis as a target for antiviral therapy. Nat Biotechnol 26:1179–1186
59. Li ZQ, Ji BW, Dixit D, Tchourine K, Lien C, Hosios M et al (2022) Cancer cells depend on environmental lipids for proliferation when electron acceptors are limited. Nat Metab 4:711
60. Chitraju C, Mejhert N, Haas T, Diaz G, Grueter A, Imbriglio E et al (2017) Triglyceride synthesis by DGAT1 protects adipocytes from lipid-induced ER stress during lipolysis. Cell Metab 26:407
61. Schott B, Weller G, Schulze J, Krueger W, Drizyte K, Casey A et al (2019) Lipid droplet size directs lipolysis and lipophagy catabolism in hepatocytes. J Cell Biol 218:3320–3335
62. Zechner R, Zimmermann R, Eichmann O, Kohlwein D, Haemmerle G, Lass A et al (2012) Lipases and lipolysis in lipid metabolism and signaling. Cell Metab 15:279–291
63. Yue Z, Hu B, Li JJ, Chen RF, Yuan Z, Xiao HR et al (2023) Coronaviral ORF6 protein mediates inter-organelle contacts and modulates host cell lipid flux for virus production. EMBO J 42:21
64. Scorrano L, De Matteis A, Emr S, Giordano F, Hajnóczky G, Kornmann B et al (2019) Coming together to define membrane contact sites. Nat Commun 10:11
65. Maekawa M, Fairn D (2014) Molecular probes to visualize the location, organization and dynamics of lipids. J Cell Sci 127:4801–4812
66. Ricciardi S, Guarino M, Giaquinto L, Polishchuk V, Santoro M, Di G et al (2022) The role of NSP6 in the biogenesis of the SARS-CoV-2 replication organelle. Nature 606:761

67. Liu YY, Liang XD, Liu CC, Cheng Y, Chen H, Baloch AS et al (2021) Fatty acid synthase is involved in classical swine fever virus replication by interaction with NS4B. J Virol 95:18

Figures

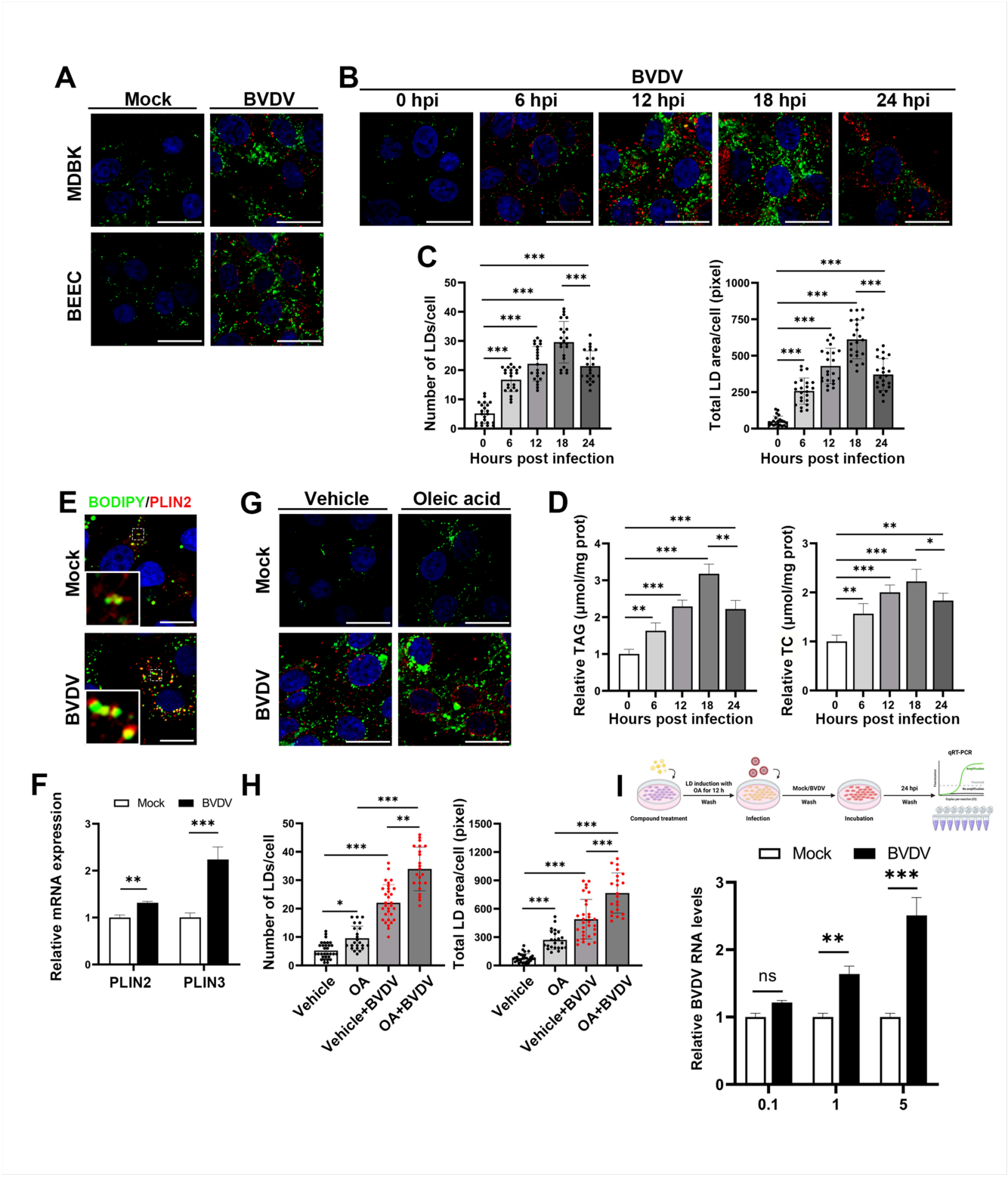


Figure 1

BVDV upregulates LD biogenesis in favor of viral replication. (A) MDBK cells and BEECs were infected with BVDV strain AV67 at an MOI of 5 and fixed at 12 hpi. All cells were stained with BODIPY 493/503 to visualize LDs (green) and DAPI to visualize the cell nuclei (blue). BVDV was detected using the anti-dsRNA (J2) antibody (red) (Cell Signaling). Images are representative of three independent experiments. Scale bar represents 20 μm. (B) MDBK cells were treated as in panel A and fixed at the indicated time points. (C) MDBK cells were treated as in panel B. The average number of LDs per cell and total LD area per cell were quantified from all time points using the “Analyze particles” function of ImageJ (more than 20 cells; n = 3 biological replicates). (D) MDBK cells were treated as in panel B. Cellular lipids were extracted, and the amounts of TAGs and TC were quantified. (E) Mock or BVDV-infected (MOI = 5) MDBK cells were incubated in a maintenance medium. At 12 hpi, cells were fixed and stained with anti-perilipin 2 (red) and BODIPY 493/503 to visualize LDs (green). The nuclei were stained with DAPI (blue). (F) MDBK cells were treated as in panel E. The mRNA expression of *PLIN2* and *PLIN3*was quantified by qRT-PCR. (G) MDBK cells were treated with 200 μM oleic acid (OA) for 12 h. Cells were stained with BODIPY 493/503 to visualize LDs (green) and DAPI to visualize the cell nuclei (blue). (H) MDBK cells were treated as in panel G. The average number of LDs per cell and total LD area per cell were quantified using the “Analyze particles” function of ImageJ (more than 20 cells; n = 3 biological replicates). (I) Schematic representation of lipid loading from oleic acid treatment to promote BVDV replication. MDBK cells were pretreated with 200 μM OA for 12 hours, followed by infection with BVDV at an MOI of 0.1, 1, and 5. qRT-PCR was used to evaluate BVDV replication at 24 hpi. Bar graphs, means ±SEM, and statistical significances were determined using unpaired Student’s *t*test or one-way ANOVA (ns, $p > 0.05$; *, $p < 0.05$; **, $p < 0.01$; ***, $p < 0.001$).

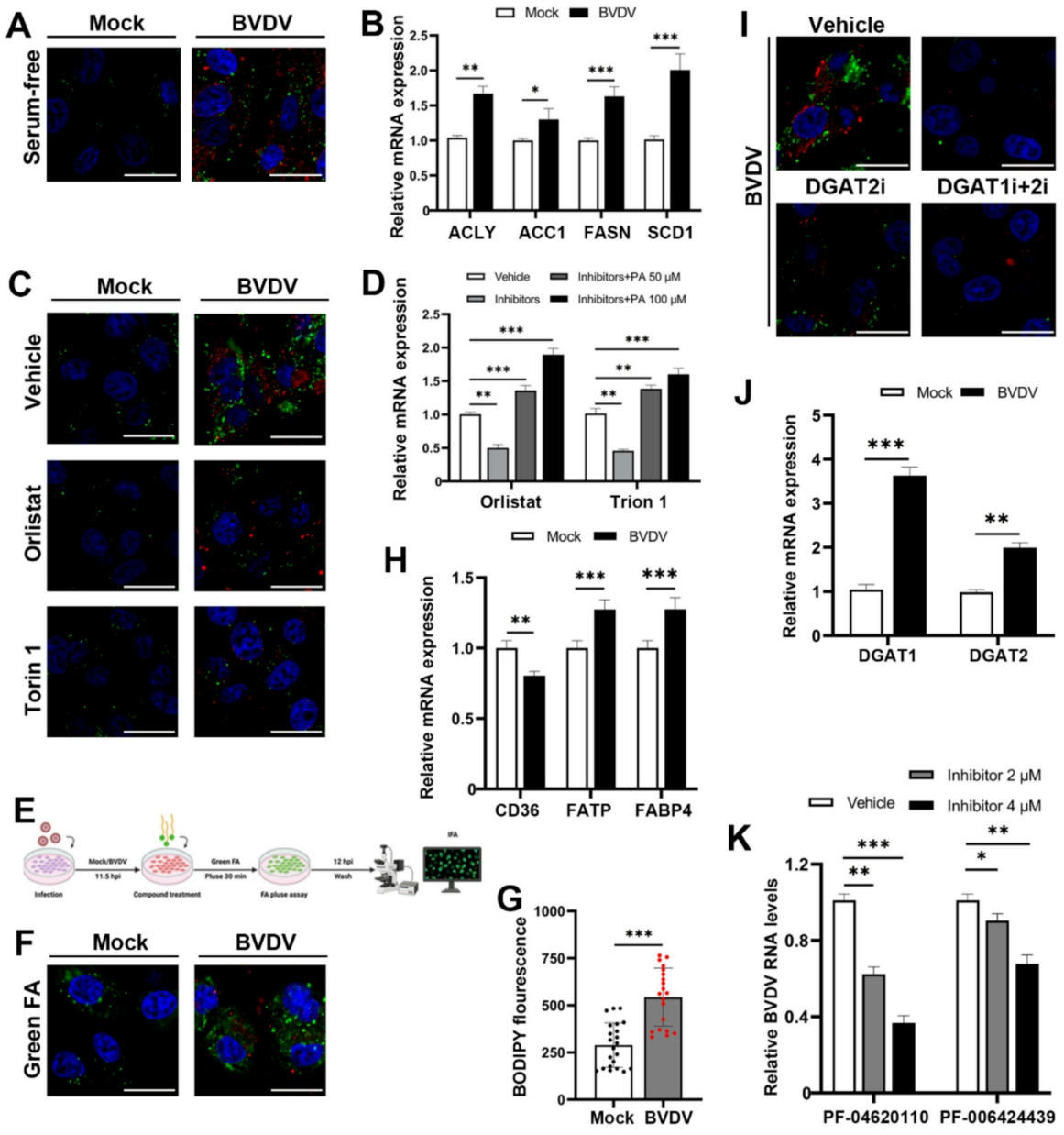


Figure 2

BVDV increases the number of cellular LDs by promoting de novo lipogenesis, exogenous fatty acid uptake, and DGAT-dependent FA esterification. (A) Mock or BVDV-infected (MOI = 5) MDBK cells were incubated in serum-free maintenance medium for exogenous fatty acid uptake. At 12 hpi, cells were fixed and stained with BODIPY 493/503 to visualize LDs (green) and DAPI to visualize the cell nuclei (blue). BVDV was detected using the anti-dsRNA (J2) antibody (red) (Cell Signaling). (B) Mock or BVDV-infected (MOI = 5) MDBK cells were incubated in a maintenance medium. qRT-PCR was used to evaluate the expression of key genes involved in DNL at 12 hpi. (C) Mock or BVDV-infected (MOI = 5) MDBK cells were incubated at 1 hpi with DMSO, 5 μM Orlistat, or 500 nM Torin 1 respectively. At 12 hpi, cells were

fixed and stained with BODIPY 493/503 to visualize LDs (green) and DAPI to visualize the cell nuclei (blue). (D) BVDV-infected (MOI = 1) MDBK cells were treated with Orlistat, Torin 1, and palmitate as indicated for 24 h. qRT-PCR was performed to detect intracellular BVDV RNA levels at 24 hpi. (E) Schematic of the fatty acid uptake test. (F-G) Mock or BVDV-infected (MOI = 5) MDBK cells were maintained in fresh phenol red-free DMEM. At 11.5 hpi, cells were incubated for 30 min in DMEM medium containing 5 μM of the BODIPY 500/510. At 12 hpi, cells were fixed and stained with DAPI to visualize the cell nuclei (blue) and fluorescence intensity of BODIPY 500/510. (H) Mock or BVDV-infected (MOI = 5) MDBK cells were incubated in a maintenance medium. qRT-PCR was used to evaluate the expression of key genes of FA uptake at 12 hpi. (I) BVDV-infected (MOI = 5) MDBK cells were incubated at 1 hpi with DMSO or 4 μM PF-04620110 or 4 μM PF-006424439 or combined PF-04620110 and PF-006424439 respectively. At 12 hpi, cells were fixed and stained with BODIPY 493/503 to visualize LDs (green) and DAPI to visualize the cell nuclei (blue). (J) Mock or BVDV-infected (MOI = 5) MDBK cells were incubated in a maintenance medium. qRT-PCR was utilized to evaluate the expression of key genes of FA esterification at 12 hpi. (K) BVDV-infected (MOI = 1) MDBK cells were treated with PF-04620110 or PF-006424439 as indicated for 24 h. qRT-PCR was performed to detect intracellular BVDV RNA levels at 24 hpi. Bar graphs, means ±SEM, and statistical significances were determined using unpaired Student's *t*test or one-way ANOVA (ns, $p > 0.05$; *, $p < 0.05$; **, $p < 0.01$; ***, $p < 0.001$).

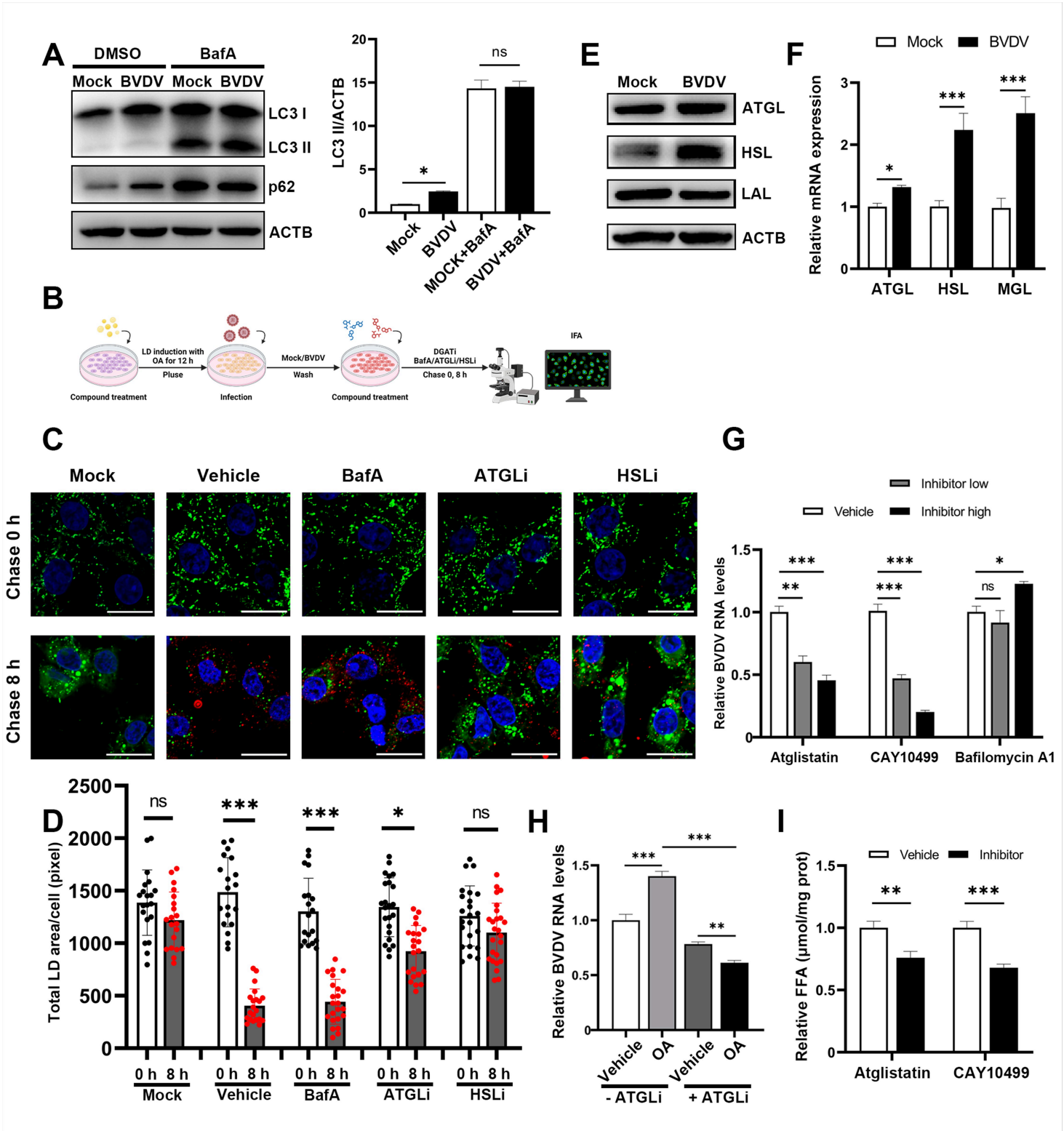


Figure 3

BVDV mobilizes LDs by promoting lipolysis rather than lipophagy. (A) Mock or BVDV-infected (MOI = 5) MDBK cells were incubated in a maintenance medium. Western blotting was used to evaluate the expression of LC3II and p62. (B) Schematic of the OA pulse-chase experiment. MDBK cells were pretreated with 200 μM OA for 12 hours and were treated with DGAT1 and DGAT2 inhibitors to suppress new LD biogenesis. After 1 h of absorption, Mock or BVDV-infected (MOI = 5) MDBK cells were incubated

at 1 hpi with DMSO or 200 nM bafilomycin A1 or 10 μM Atglistatin or 10 μM CAY10499. (C) MDBK cells were treated as in panel B. At 1 hpi and 9 hpi, cells were fixed and stained with BODIPY 493/503 to visualize LDs (green) and DAPI to visualize the cell nuclei (blue). BVDV was detected using the anti-dsRNA (J2) antibody (red) (Cell Signaling). Images are representative of three independent experiments. (D) MDBK cells were treated as in panel B. The total LD area per cell was quantified using the “Analyze particles” function of ImageJ (more than 20 cells; n = 3 biological replicates). (E-F) Mock or BVDV-infected (MOI = 5) MDBK cells were incubated in a maintenance medium. Western blotting and qRT-PCR were used to evaluate the expression of key genes of lipolysis and lipophagy. (G) BVDV-infected (MOI = 1) MDBK cells were treated with Atglistatin, CAY10499, and bafilomycin A1 as indicated for 24 h. qRT-PCR was performed to detect intracellular BVDV RNA levels at 24 hpi. (H) MDBK cells were pretreated with 200 μM OA for 12 hours before infection with BVDV (MOI = 1), and cells were incubated at 1 hpi with DMSO or 5 μM CAY10499 respectively. qRT-PCR was performed to detect intracellular BVDV RNA levels at 24 hpi. (I) MDBK cells were treated as in E. Cellular lipids were extracted, and the amount of free fatty acid was quantified. Bar graphs, means ± SEM, and statistical significances were determined using unpaired Student’s *t* test or one-way ANOVA (ns, $p > 0.05$; *, $p < 0.05$; **, $p < 0.01$; ***, $p < 0.001$).

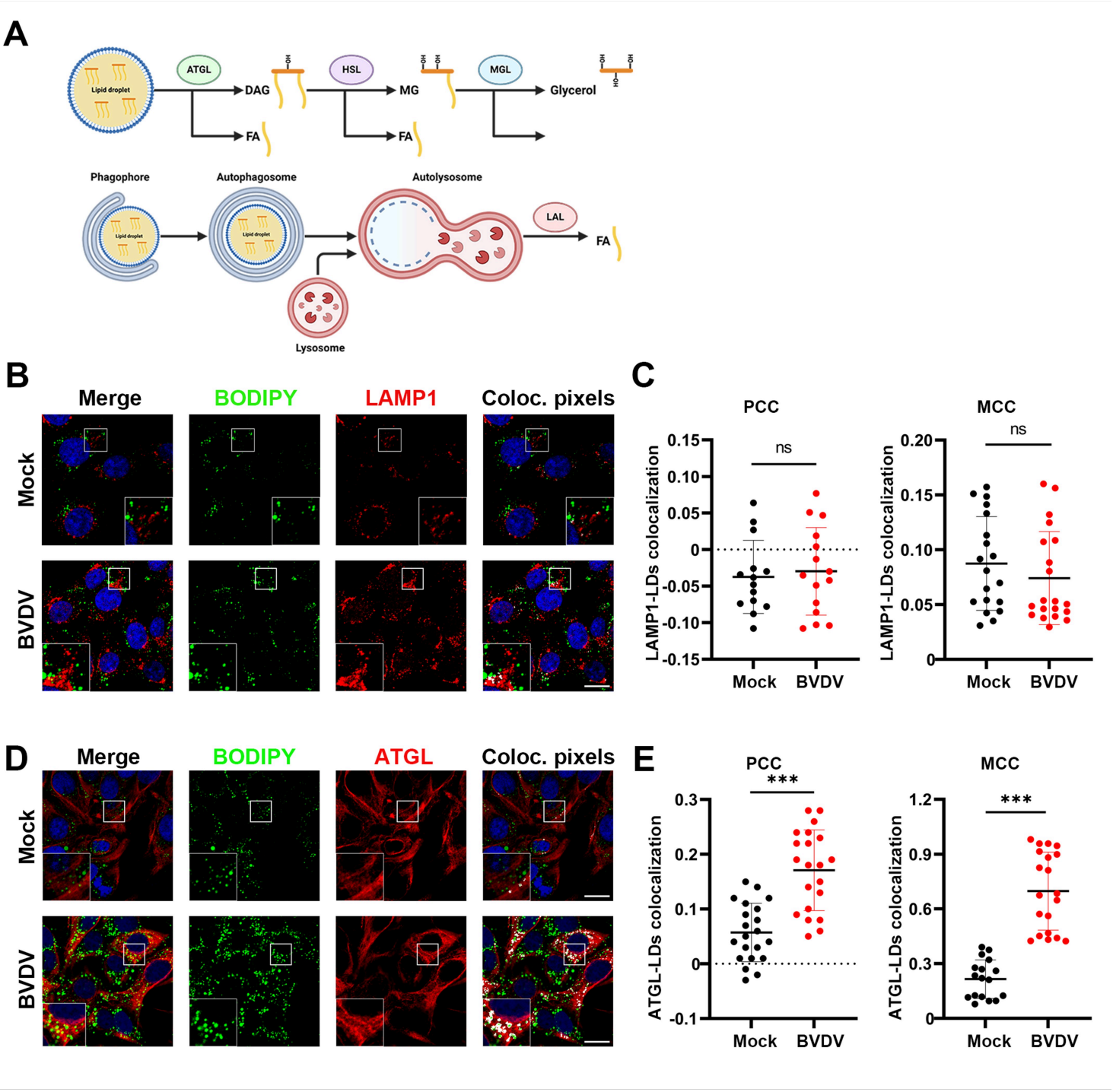


Figure 4

BVDV enhances the interaction between neutral lipase and LDs instead of increasing LD turnover in lysosomes. (A) Schematic of lipolysis and lipophagy. (B) Mock or BVDV-infected (MOI = 5) MDBK cells were incubated in a maintenance medium. At 12 hpi, cells were fixed and stained with an anti-LAMP1 antibody to visualize lysosomes (red) and BODIPY 493/503 to visualize LDs (green). The nuclei were stained with DAPI (blue). The rightmost image shows the co-localized pixels as white. (C) Quantification of the colocalization of lysosomes and LDs by calculation of the PCC and MCC between signals in the red and green channels in experimental and control alignments (more than 20 cells; n = 3 biological

replicates). (D) Mock or BVDV-infected (MOI = 5) MDBK cells were incubated in a maintenance medium. At 12 hpi, cells were fixed and stained with an antibody to ATGL (red) and BODIPY 493/503 to visualize LDs (green). The nuclei were stained with DAPI (blue). The rightmost image shows the co-localized pixels as white. (E) Quantification of the colocalization of ATGL and LDs by calculation of the PCC and MCC between signals in the red and green channels in experimental and control groups (more than 20 cells; n = 3 biological replicates).

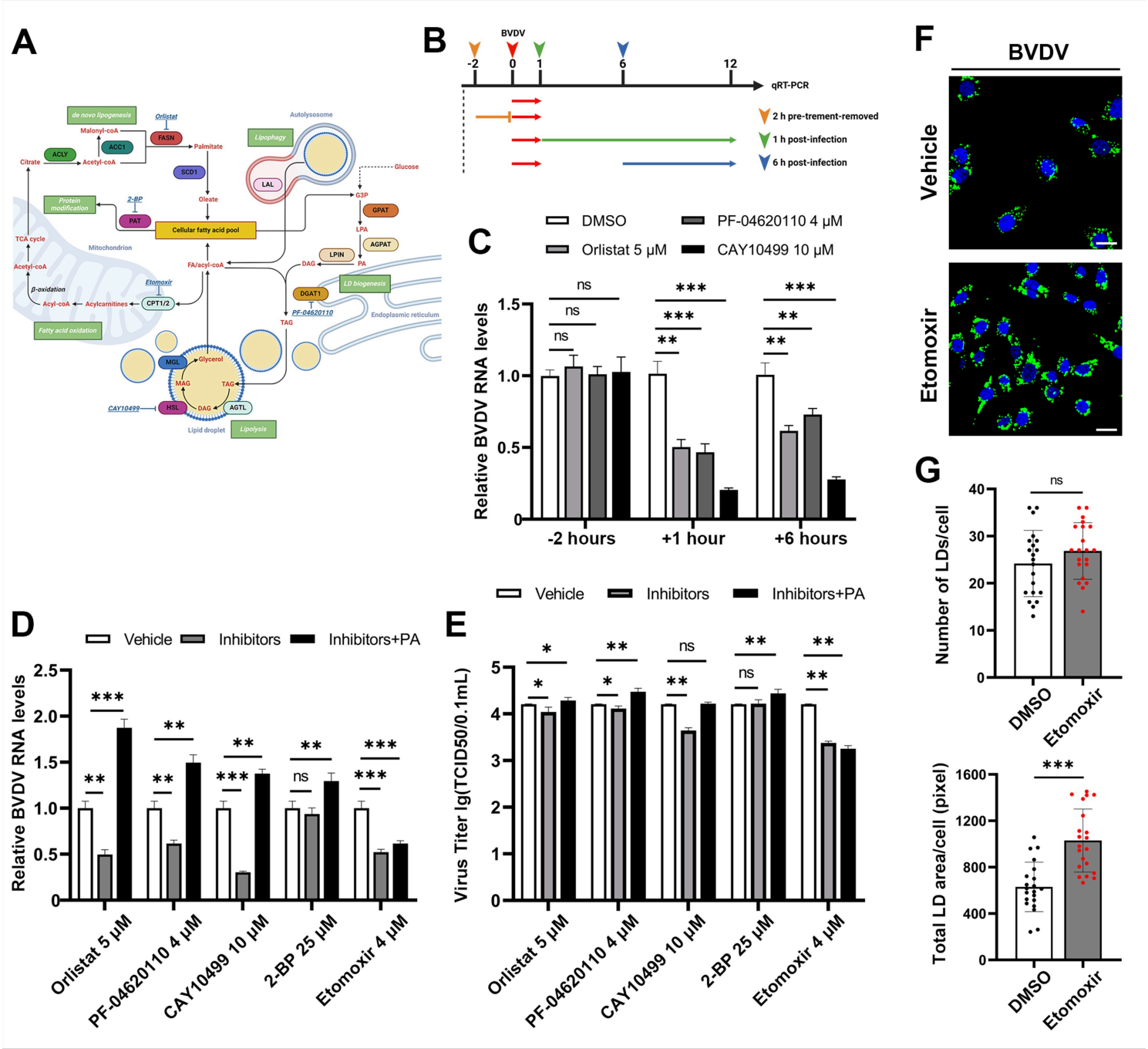


Figure 5

Regulation of lipid metabolism to beta-oxidative pathways is critical for BVDV replication. (A) Schematic of neutral lipid metabolism. GPAT, glycerol-3-phosphate acyltransferase; AGPAT, 1-

acylglycerol-3-phosphate O-acyltransferase; LPIN, phosphatidate phosphatase LPIN1; G3P, glycerol-3-phosphate; LPA, lysophosphatidic acid; PA, phosphatidic acid; PC, phosphatidylcholine; PS, phosphatidylserine; PE, phosphatidylethanolamine; PI, phosphatidylinositol; 2-BP, 2-bromopalmitate; PAT, palmitoyl acyltransferase. (B) Timeline for the time-of-addition experiment. MDBK cells were either pre-treated for two hours with compounds, which were then removed prior to infection (-2) or treated at 1 (+1) or 6 (+6) hours post infection. (C) qRT-PCR was performed to detect intracellular BVDV RNA levels at 12 hpi. (D) BVDV-infected (MOI = 1) MDBK cells were treated with Orlistat, PF-04620110, CAY10499, 2-BP, Etomoxir, and palmitate as indicated for 24 h. qRT-PCR was performed to detect intracellular BVDV RNA levels at 24 hpi. (E) BVDV-infected MDBK cells (MOI = 1) were treated with inhibitors as described for panel D. $TCID_{50}$ was performed to detect viral titers at 24 hpi. (F) BVDV-infected (MOI = 5) MDBK cells were incubated at 1 hpi with DMSO or 4 μM etomoxir respectively. At 12 hpi, cells were fixed and stained with BODIPY 493/503 to visualize LDs (green) and DAPI to visualize the cell nuclei (blue). (G) MDBK cells were treated as described for panel F. The average number of LDs per cell and total LD area per cell were quantified using the “Analyze particles” function of ImageJ (more than 20 cells; n = 3 biological replicates). Bar graphs, means ± SEM, and statistical significances were determined using unpaired Student’s *t* test or one-way ANOVA (ns, $p > 0.05$; *, $p < 0.05$; **, $p < 0.01$; ***, $p < 0.001$).

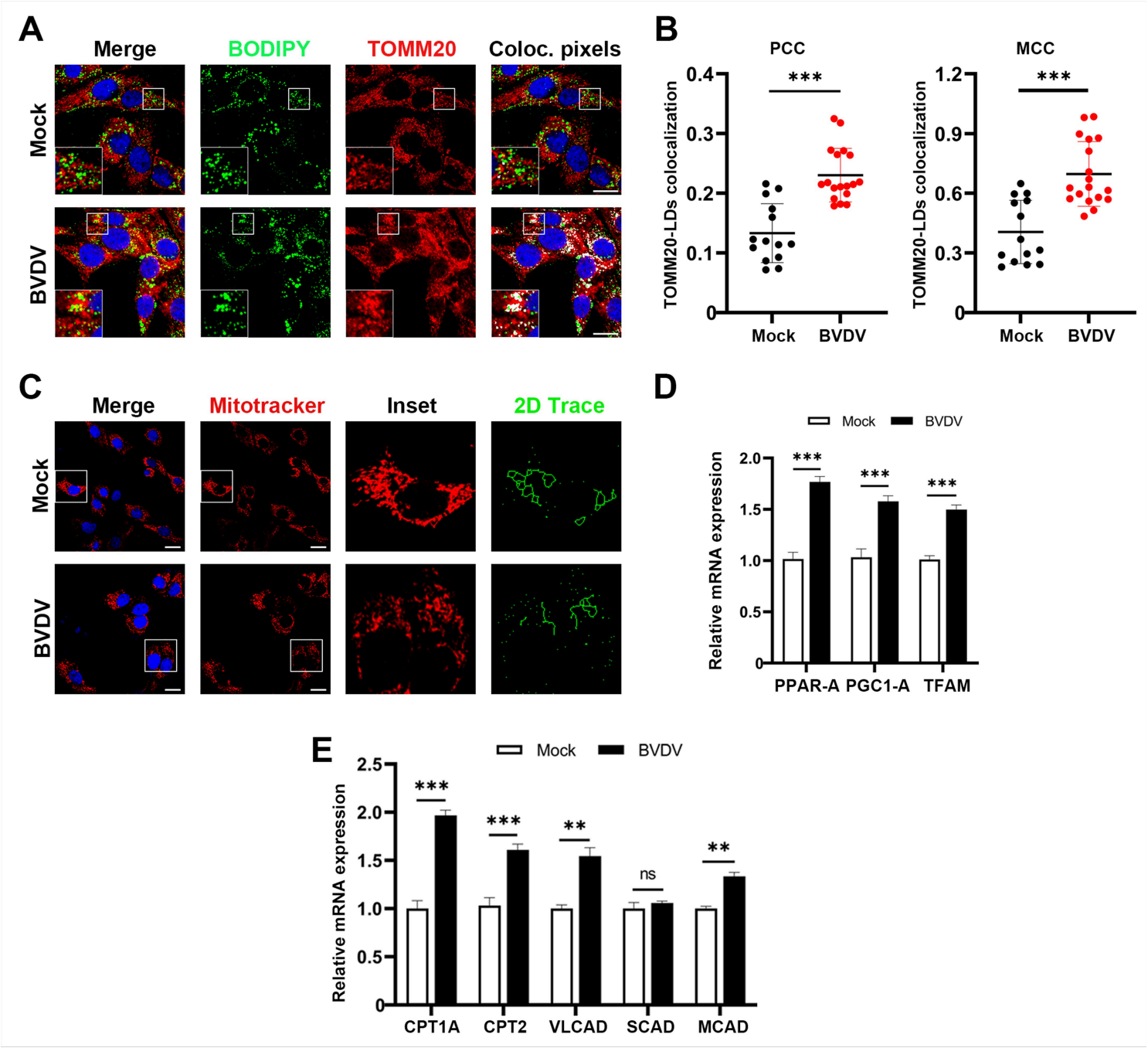


Figure 6

BVDV promotes the proximity of LDs to the mitochondrial network and enhances fatty acid oxidation. (A) Mock or BVDV-infected (MOI = 5) MDBK cells were incubated in a maintenance medium. At 12 hpi, cells were fixed and stained with an antibody to TOMM20 (red) to visualize mitochondria and BODIPY 493/503 to visualize LDs (green). The nuclei were stained with DAPI (blue). The rightmost image shows the co-localized pixels as white. Images are representative of three independent experiments. (B) Quantification of the colocalization of TOMM20 and LDs by calculation of the PCC and MCC between signals in the red and green channels in experimental and control groups (more than 20 cells; n = 3 biological replicates). (C) Mock or BVDV-infected (MOI = 5) MDBK cells were incubated in a maintenance medium. At 12 hpi, cells were fixed and stained with Mito-Tracker to visualize mitochondria (red) and

DAPI to visualize the cell nuclei (blue). The rightmost image represents the 2D trace of the tubular mitochondrial network obtained by the Skeletonize 2D/3D plugin of ImageJ. Images are representative of three independent experiments. (D) MDBK cells were treated as in panel C. qRT-PCR was used to evaluate the expression of key genes involved in mitochondrial biogenesis at 12 hpi. (E) MDBK cells were treated as in panel C. qRT-PCR was used to evaluate the expression of key genes involved in mitochondrial fatty acid beta-oxidation at 12 hpi. Bar graphs, means ± SEM, and statistical significances were determined using unpaired Student's *t* test or one-way ANOVA (ns, $p > 0.05$; *, $p < 0.05$; **, $p < 0.01$; ***, $p < 0.001$).

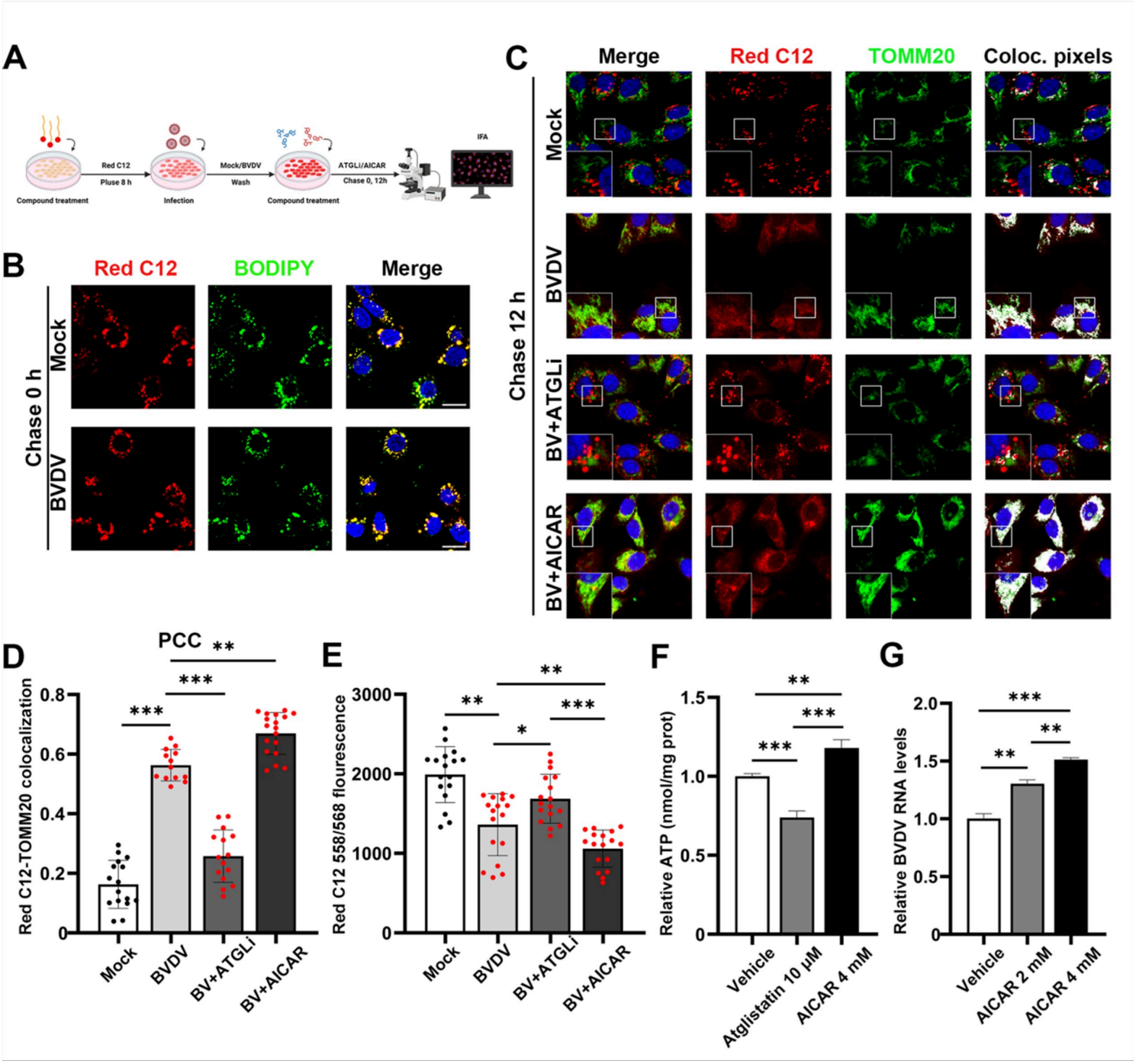


Figure 7

BVDV accelerates the transfer of FAs from LDs to mitochondria. (A) Schematic representation of the Red C12 pulse-chase assay. MDBK cells were pulsed with Red C12 for 8 h to allow the dye to accumulate in LDs. After 1 h of absorption, BVDV-infected (MOI = 5) MDBK cells were incubated at 1 hpi with DMSO, 10 μM Atglistatin, or 4 mM AICAR respectively. Cells were then chased in DMEM supplemented with 1% FBS for 12 hours and imaged to determine the subcellular localization of the FAs. (B) MDBK cells were treated as described in panel A. At 0 hpi, cells were fixed and stained with BODIPY 493/503 to visualize LDs (green) and DAPI to visualize the cell nuclei (blue). Images are representative of three independent experiments. (C) MDBK cells were treated as described in panel A. At 12 hpi, Confocal fluorescence microscopy of MDBK cells stained with TOMM20 to visualize mitochondria (green) and DAPI to visualize the cell nuclei (blue). The rightmost image shows the co-localized pixels as white. Images are representative of three independent experiments. (D) Quantification of the colocalization of Red C12 and mitochondria by calculation of the PCC between signals in the red and green channels in experimental and control groups (more than 20 cells; n = 3 biological replicates). (E) Total Red C12 fluorescence per cell was quantified using ImageJ (more than 20 cells; n = 3 biological replicates). Bar graphs, means ± SEM, and statistical significances were determined using unpaired Student's *t* test or one-way ANOVA (ns, $p > 0.05$; *, $p < 0.05$; **, $p < 0.01$; ***, $p < 0.001$). (F) MDBK cells were pulsed with Red C12 for 8 h to allow the Red C12 to accumulate in LDs. After 1 h of absorption, BVDV-infected (MOI = 5) MDBK cells were incubated at 1 hpi with DMSO, 10 μM Atglistatin, or 4 mM AICAR. Cells were then chased in DMEM supplemented with 1% FBS for 12 hours and the amount of ATP was quantified. (G) MDBK cells were treated as in F. After 1 h of absorption, BVDV-infected (MOI = 1) MDBK cells were treated with AICAR as indicated for 24 h. qRT-PCR was performed to detect intracellular BVDV RNA levels at 24 hpi.

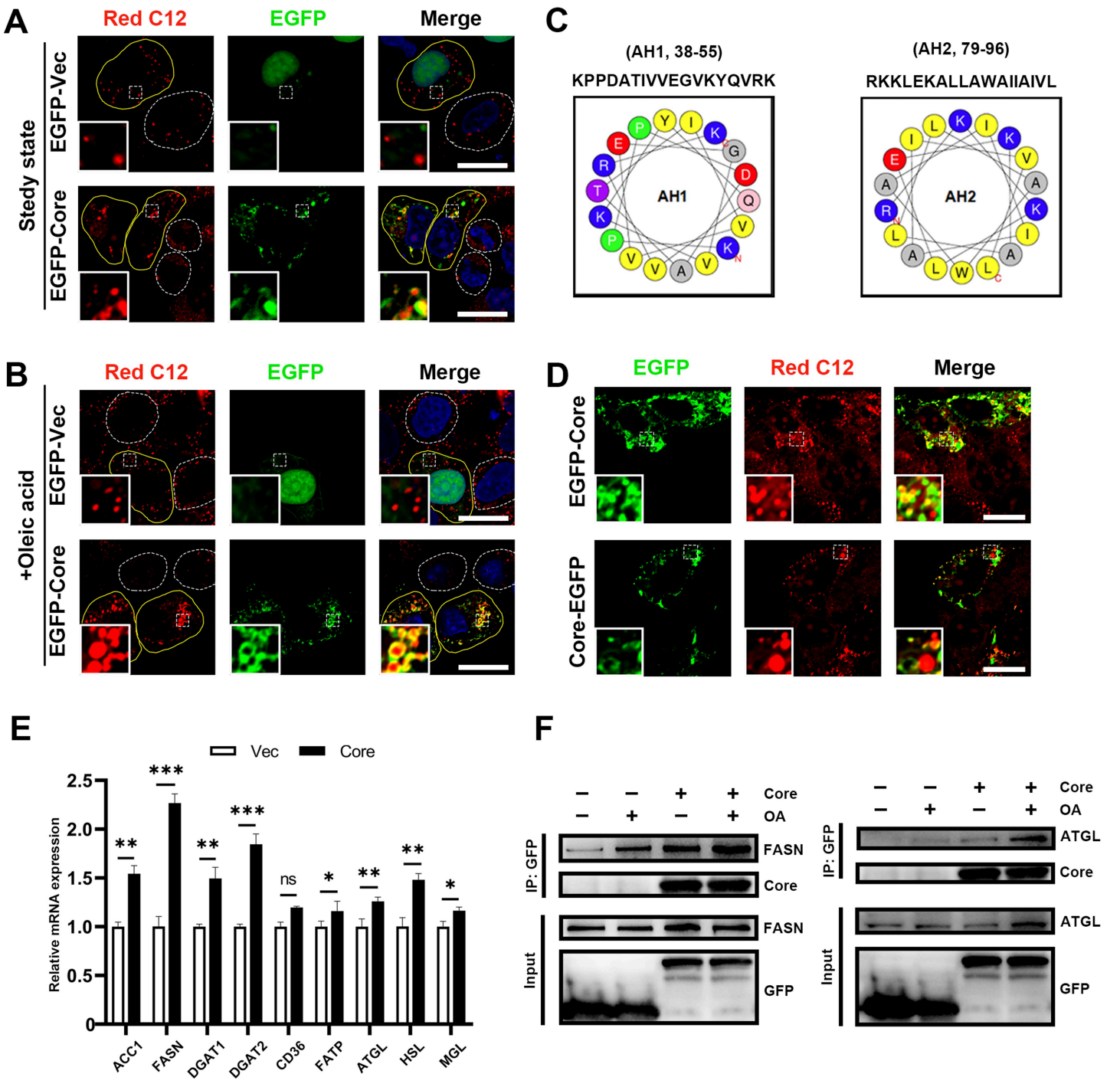


Figure 8

BVDV Core protein targets LDs to promote the mobilization of LDs. (A) Cells were transfected with pEGFP-C1 or pEGFP-Core plasmid for 12 h and LDs were labeled with Red C12 (red). At 24 hpi, cells were fixed and stained with DAPI to visualize the nuclei (blue). Images are representative of three independent experiments. (B) Cells were treated as in panel A and treated with 200 μM OA for another 12 h. LDs were labeled with Red C12 (red). At 24 hpi, cells were fixed and stained with DAPI to visualize the cell nuclei (blue). Images are representative of three independent experiments. (C) The two predicted amphipathic helical domains of residues 38-55 (AH1) and residues 79-96 (AH2) of BVDV Core protein were generated

via the HeliQuest tool. (D) Cells were transfected with pCore-EGFP or pEGFP-Core plasmid for 12 h and treated with 200 μM OA for another 12 h. LDs were labeled with Red C12 (red). At 24 hpi, cells were fixed and stained with DAPI to visualize the cell nuclei (blue). Images are representative of three independent experiments. (E) Cells were treated as in panel A. qRT-PCR was used to evaluate the expression of key genes involved in lipid metabolism at 24 hpi. Bar graphs, means ±SEM, and statistical significances were determined using unpaired Student's *t*test or one-way ANOVA (ns, $p > 0.05$; *, $p < 0.05$; **, $p < 0.01$; ***, $p < 0.001$). (F) Cells were transfected with pEGFP-C1 or pEGFP-Core plasmid for 12 h and treated with 200 μM OA for another 12 h. At 36 h, protein interactions were detected by immunoprecipitation using anti-EGFP magnetic agarose beads and immunoblotting analysis with FASN and ATGL antibodies.

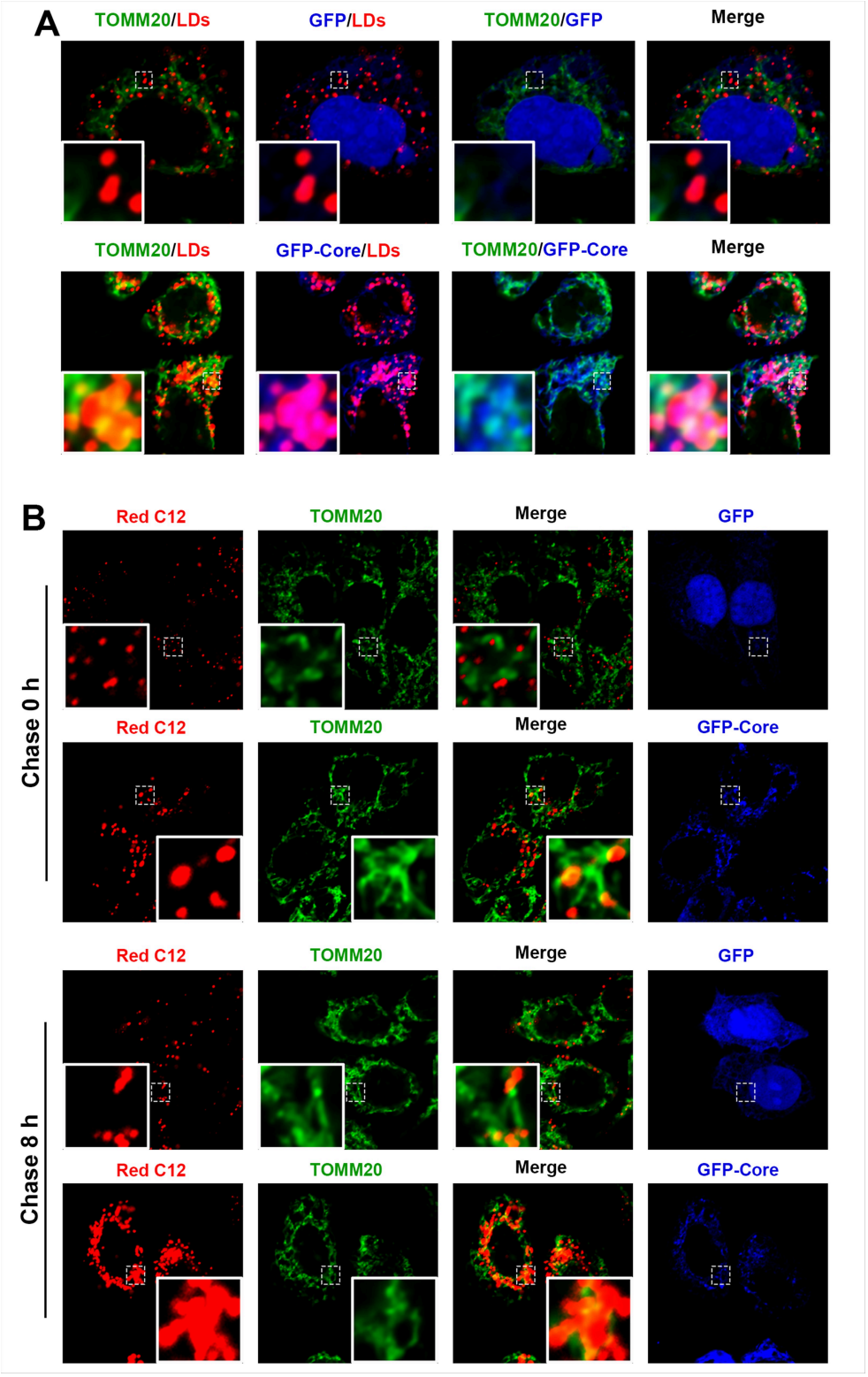


Figure 9

BVDV Core protein links mitochondria to LDs. (A) Cells were transfected with pEGFP-C1 or pEGFP-Core (blue) plasmid for 12 h, and LDs were labeled with Red C12 (red). At 24 hpi, cells were fixed and stained with anti-TOMM20 to visualize the mitochondria (green). Images are representative of three independent experiments. Scale bar represents 20 μm. (B) Pulse-chase assays were performed in vector or EGFP-Core expressing cells. HeLa cells were incubated in complete medium containing 1 μM BODIPY 558/568

C12 (red) for 16 h. Cells were washed with PBS three times and then chased (0 h) or no-chased in EBSS for 8 h, and then were fixed and stained with anti-TOMM20 (green). Images are representative of three independent experiments. Scale bar represents 20 μm.

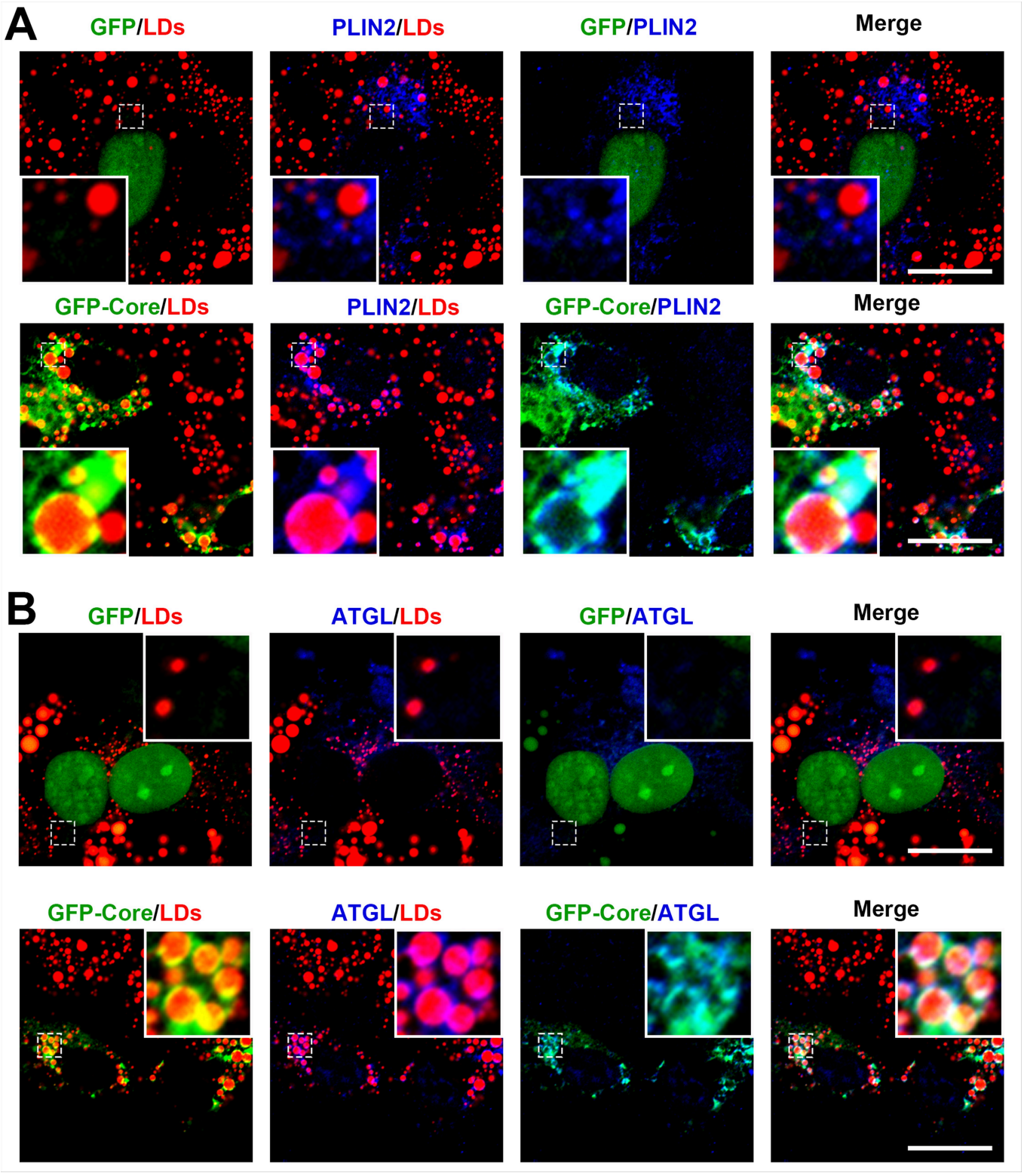


Figure 10

Core recruits ATGL to the surface of lipid droplets. (A) Co-transfection of cells with p-EGFP-C1/pEGFP-Core and pCMV-PLIN2-FLAG for 12 h, and LDs were labeled with Red C12 (red). At 24 hpi, cells were fixed and stained with a fluorescent secondary antibody to detect PLIN2 (blue). Images are representative of three independent experiments. (B) Co-transfection of cells with p-EGFP-C1/pEGFP-Core and pCMV-ATGL-HA for 12 h, and LDs were labeled with Red C12 (red). At 24 hpi, cells were fixed and stained with a fluorescent secondary antibody to detect ATGL (blue). Images are representative of three independent experiments.

Supplementary Files

This is a list of supplementary files associated with this preprint. Click to download.

- S1Fig.tif.tif
- S2Fig.tif.tif
- S3Fig.tif.tif
- S4Fig.tif.tif
- S5Fig.tif.tif